8-30-2011

Thermal detection in the long wave infrared and very long wave infrared regions

Emil Kadlec

Emil A. Kadlec
Candidate

Electrical Engineering
Department

This thesis is approved, and it is acceptable in quality and form for publication:

Approved by the Thesis Committee:

Charles B. Fleddermann, Chairperson

Eric Shaner

Mani Hossein-Zadeh

THERMAL DETECTION IN THE LONG WAVE INFRARED AND VERY LONG WAVE INFRARED REGIONS

BY

EMIL A. KADLEC

B.S., ELECTRICAL ENGINEERING
UNIVERSITY OF NEW MEXICO, 2008

THESIS

Submitted in Partial Fulfillment of the
Requirements for the Degree of

Master's of Science
Electrical Engineering

The University of New Mexico
Albuquerque, New Mexico

May, 2011

Dedication

To my fiancé Mallory Yoder, thank you for your support and help through the course of earning this degree.

To my mother, father, and brother, thank you for always having my back.

To Dr. Eric Shaner, thank you for taking a risk on me, without you this would not have been possible.

Acknowledgment

I would like to give a special thanks to Todd Barrick and Jeremy Wright who have always gone out of their way to help me. I would also like to acknowledge and thank my thesis committee members, Dr. Charles Fleddermann, Dr. Eric Shaner, and Dr. Mani Hossein-Zadeh.

This work was performed at Sandia National Laboratories. Sandia National Laboratories is a multi-program laboratory operated by Sandia Corporation, a Lockheed-Martin Company, for the U. S. Department of Energy under Contract No. DE-AC04-94AL85000.

THERMAL DETECTION IN THE LONG WAVE INFRARED AND VERY LONG WAVE INFRARED REGIONS

BY

EMIL A. KADLEC

ABSTRACT OF THESIS

Submitted in Partial Fulfillment of the
Requirements for the Degree of

Master's of Science
Electrical Engineering

The University of New Mexico
Albuquerque, New Mexico

May, 2011

THERMAL DETECTION IN THE LONG WAVE INFRARED AND VERY LONG WAVE INFRARED REGIONS

By

Emil A. Kadlec

B.S., Electrical Engineering, University of New Mexico, 2008
M.S., Electrical Engineering, University of New Mexico, 2011

ABSTRACT

Thermal detection has made extensive progress in the last 40 years, however, the speed and detectivity remain insufficient for certain applications. The advancement of microphotonic resonators has brought interest of their use as detection devices due to their small size and high quality factors. Implementing silicon photonic microring resonators as a means of a thermal detector gives rise to higher speed and detectivity, as well as lower noise. Thermal detection in the far wave infrared region (Terahertz) remains underdeveloped, opening a door for new innovative technologies such as metamaterials. This thesis will present the design and measurements of silicon photonic microring resonators used for thermal detection. The characteristic values, consisting of the thermal time constant ($\tau \approx 2\ ms$) and noise equivalent power (NEP $\approx 10^{-12}\ W/\sqrt{Hz}$), were measured and found to surpass the performance of the best microbolometers. Furthermore the detectivity was found to be $D_\lambda = 1.8 \times 10^8\ cm \cdot \sqrt{Hz}/W$; this is comparable to commercial detectors. Subsequent design modifications should increase the detectivity by another order of magnitude. Also shown is the use of metamaterials in conjunction with a bimorph cantilever design for detection in the far wave infrared region. While much work remains to institute these technologies into a deployable product, the early stages of research show potential for use in thermal detection and other applications.

Table of Contents

Table of figures

Chapter 1

1.1 Motivation

Thermal detection has grown tremendously over the past 40 years due to the enormous amount of progress in microsystems technology, leading to an overall decrease in the cost of fabrication and size, as well as the increase in sensitivity of thermal detectors. Within the numerous applications of thermal detection a key area is thermal imaging, which is used in reducing energy costs of buildings, detection of gaseous species, medicine, veterinary and many other fields [2-6]. Although thermal detection has seen considerable development, commercial detectors, such as bolometers can be improved in terms of speed and detectivity. Another related area for improvement is the far-infrared or terahertz (THz) detection and imaging, which is mainly done using a scanning time domain spectroscopy (TDS) technique. THz imaging is currently slow but offers many useful characteristics such as the transparency of many visibly opaque materials and its nondestructive nature due to low photon energy [1]. Advancement of these fields could be made with the introduction of new technologies being implemented into focal imaging arrays.

This thesis will present two different detector technologies. The first detector to be presented, the microphotonic thermal detector, is based on silicon photonic microdisk resonators and is designed for detection in the long-wave infrared (LWIR) region (further discussion in chapter 2). The second technology, the metamaterial bimorph cantilever detector, uses a combination of metamaterials and

microelectricalmechanical (MEMs) bimorph cantilevers to detect radiation in the very-long-wave infrared (VLWIR) region. By using the resonance properties of metamaterials, heat is supplied to the bimorph arms of the cantilever device causing bending which is translated into a photoresponse (further discussion in chapter 4). The goal of this research is to characterize the two separate thermal detection technologies and to show their potential for future use. It will be shown that the microphotonic thermal detector, in its early design stages, surpasses microbolometer technology in speed, noise, and size, making it desirable for high-speed high-resolution imaging applications. Also presented is the potential of the metamaterial detector for use in detection and imaging of regions devoid of naturally occurring absorbers. The final chapter will discuss ideas for future work, such as combining silicon photonics and metamaterials, which could provide ultra-fast low-noise thermal detection of THz radiation, a field which is underdeveloped.

The following chapter will introduce basic concepts of infrared detection as well as the metrics of thermal detectors. An explanation for the importance of the LWIR region will be made and show why thermal detection is needed in this region. Also shown are the limitations of current commercially available thermal detectors and what areas are needed to be improved. This first chapter will set a basis for the fundamentals of thermal detection in the two desired regions.

1.2 Infrared Radiation

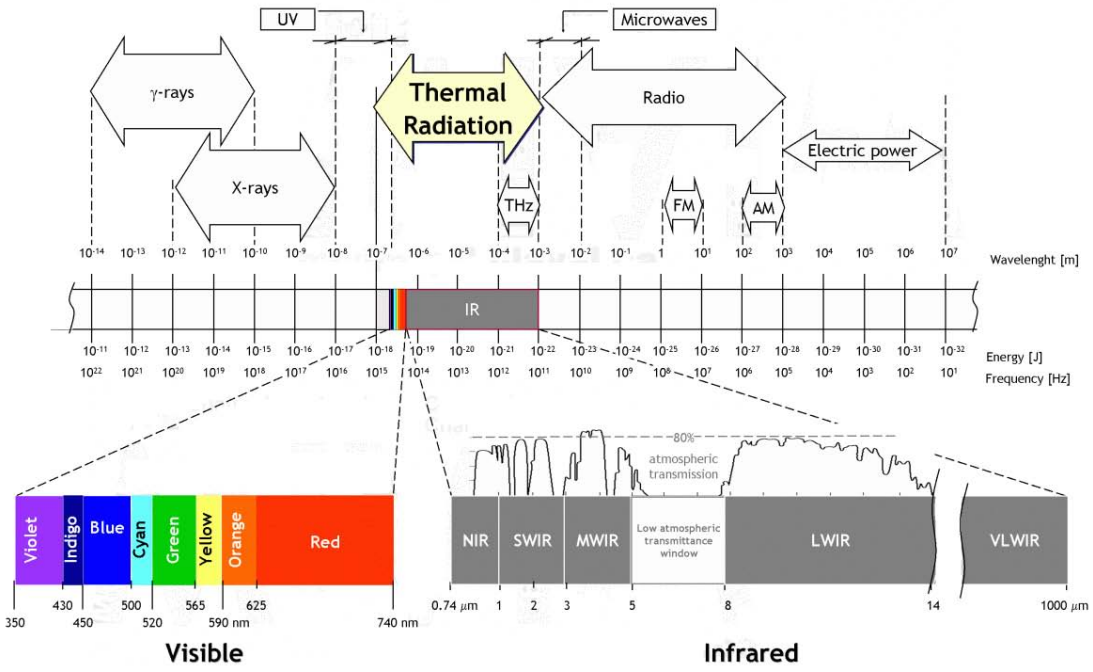

Figure 1.1: Electromagnetic Spectrum [7]

Figure 1.1 shows an overview of the electromagnetic (EM) spectrum. The visible range of the human eye occupies relatively small portion of the EM spectrum; it resides in the range of 380 – 780 nm. Radio wavelengths are defined as one millimeter and larger. The IR spectrum is defined as 780 nm – 1 mm. The terahertz (THz) spectrum, or very long wave infrared (VLWIR), ranges from 100 µm to 1 mm. The wavelengths most desirable for detection range from 3 – 20 µm. The restriction to these wavelengths follows from

consideration of the amount of thermal radiation to be expected, from the environmental blackbody radiation and from the transmission properties of the atmosphere.

1.3 Black Body Radiation

Every object emits thermal radiation when its temperature is above absolute zero (0 K). The spectrum of this radiation is described by Plank's Law of blackbody radiation. Blackbodies resemble ideal surfaces having the following properties: (1) A blackbody absorbs all incident radiation, regardless of wavelength and direction (2) For a given temperature and wavelength, no surface can emit more energy than a blackbody (3) Radiation emitted by a blackbody depends on wavelength; however, its radiance does not depend on direction [2]. As nearly perfect absorbers and emitters, blackbodies serve as standards in thermal detection. The blackbody spectrum was experimentally measured in the late 19th century, but the measured spectrum was not satisfactorily explained until Max Planck introduced his concept of quantization of energy, thus introducing an entirely new concept to the field of physics [8]. Equation 1-1 is known today as Plank's Law where $\hbar$ is Planck's constant, c is the speed of light, λ is the wavelength of the emitted radiation, k_B is Boltzmann's constant, and T is the temperature of the blackbody.

Equation 1-1

$$M(T) = \frac{2\pi\hbar c^3}{\lambda^5}\frac{1}{e^{\frac{\hbar c}{\lambda k_B T}} - 1}$$

Figure 1.2 shows the radiance in arbitrary units for blackbodies of specified temperatures. Solving Equation 1-1 for the peak wavelength gives Wien's displacement law (Equation 1-2).

Equation 1-2

$$\lambda_{PEAK} = \frac{2897.8}{T}\ \mu m \cdot K$$

The surface temperature of the Sun is around 6000 K corresponding to a blackbody peak wavelength of 500 nm. For a blackbody at environmental temperatures, T ≈ 300 K, the peak wavelength is 10 µm well outside the visible range of the human eye. Figure 1.2 shows the blackbody curves for environmental temperatures and the Sun.

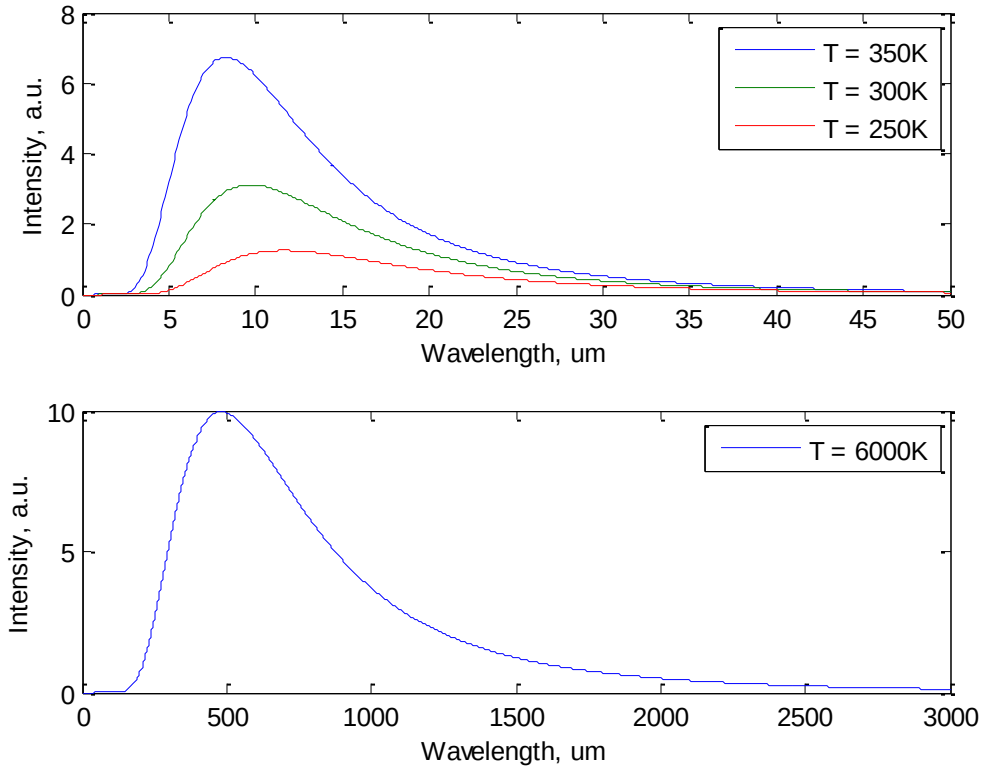

Figure 1.2: Blackbody Radiation Spectrum for T = 250K, 300K, 350K, and 6000K

Blackbodies are idealizations and no real object can emit this maximum thermal radiation except for the special case of stars. The real thermal radiation can be found by a simple multiplication of Equation 1-1 by the emissivity (ε), which describes the ratio of the actual amount of thermal radiation emitted by an object to the theoretical blackbody at the same temperature. For most practical materials of interest in thermal detection, the emissivity is constant for all of the spectral range. Objects with a constant emissivity with respect to wavelength are referred to as gray bodies. The major determinant of emissivity is the type of material. In a simplified classification, one can separately discuss nonmetals and metals. Nonmetallic materials generally possess fairly high emissivity values, $\varepsilon \approx 0.8$, and their thermal radiation spectrum resembles a gray body. These materials include skin, paper, paints, stones, glass, and so on. Metals generally possess small emissivity, $\varepsilon \approx 0.2$, because of their smooth nature and low absorbance, therefore being hard to detect. When the metallic surface is roughened the emissivity can be dramatically increased.

1.4 Atmospheric Absorption

In thermal detection, radiation must pass through a medium before being absorbed by the detector. The atmosphere is composed of several different molecules which lead to the absorption of IR radiation. Atmospheric IR absorption is mainly due to multi-atomic species, for example CO_2, CO, NO, and H_2O [2]. Figure 1.3 plots the atmospheric transmission for a 1 km path length. It can be seen from Figure 1.3 that the resultant spectrum has many bands but is mainly comprised of the LWIR region (8 – 14μm). H_2O concentration tends to change more than other atmospheric molecules with weather

patterns and geographical location, therefore the transmission spectrum tends to change at different geographical locations and weather status.

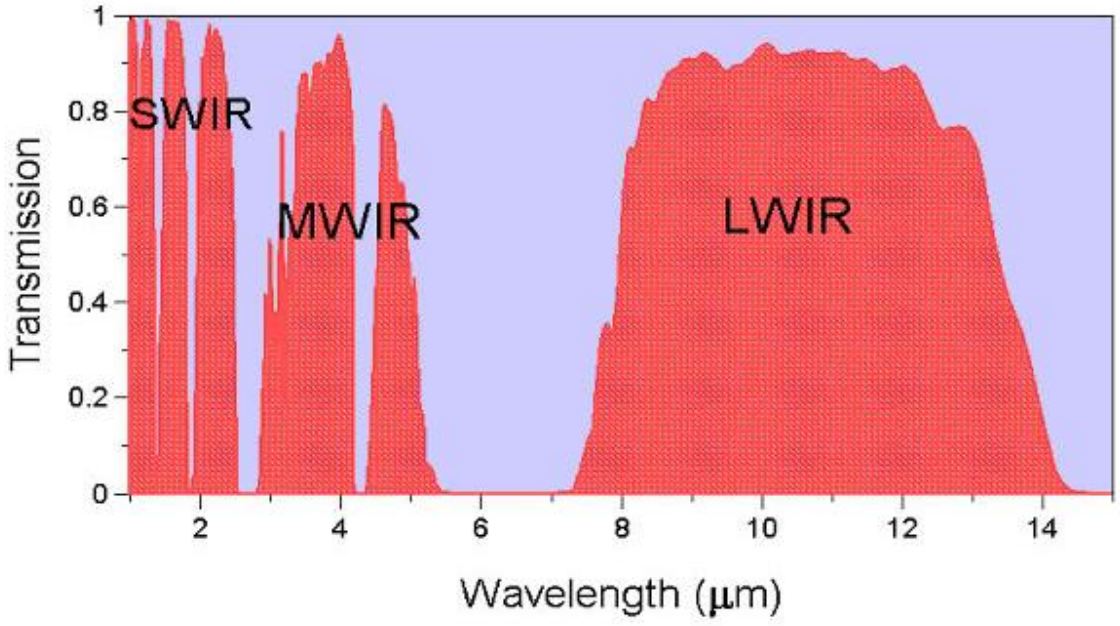

Figure 1.3: Atmospheric IR transmission for a path length of 1km [9]

1.5 Thermal Detectors

Thermal detectors convert the absorbed thermal radiation into an electrical signal by means of a temperature change in the detector. The efficiency of this technique is dependent on the absorbance of the detector and the efficiency of converting the change in detector temperature to a readout signal [2]. The energy conversion of a thermal detector can be expressed by Equation 1-3 where ΔT is the change in temperature of the detector, α is the absorbance coefficient, Φ is the radiant power, C_{th} is the heat capacitance, and G_{th} is the thermal conductance between the absorber and substrate which is considered as a heat sink [2].

Equation 1-3 $$\alpha\Phi = \mathrm{C}_{th}\frac{\partial\Delta\mathrm{T}}{\partial\mathrm{t}} + G_{th}\Delta T$$

In laboratory settings the radiation source is generally chopped via square-wave modulation. Dividing Equation 1-3 by G_{th} and then solving for the ΔT due to absorbed radiation gives Equation 1-4 for raising ΔT and Equation 1-5 for a decaying ΔT.

Equation 1-4 $$\Delta T = \frac{\alpha\Phi}{G_{th}}(1 - e^{-\frac{t}{\tau}})$$

Equation 1-5 $$\Delta T = \frac{\alpha\Phi}{G_{th}}e^{-\frac{t}{\tau}}$$

Figure 1.4 shows an ideal plot of the change in temperature of a thermal detector with an incident square-wave pulse of thermal radiation. The time constant τ is a measure of the speed of the detector. This physical characteristic explains how fast the detector responds to thermal stimulus; τ is calculated as the ratio of the heat capacitance to the heat conductance of the detector, Equation 1-6.

Equation 1-6 $$\tau = \frac{C_{th}}{G_{th}}$$

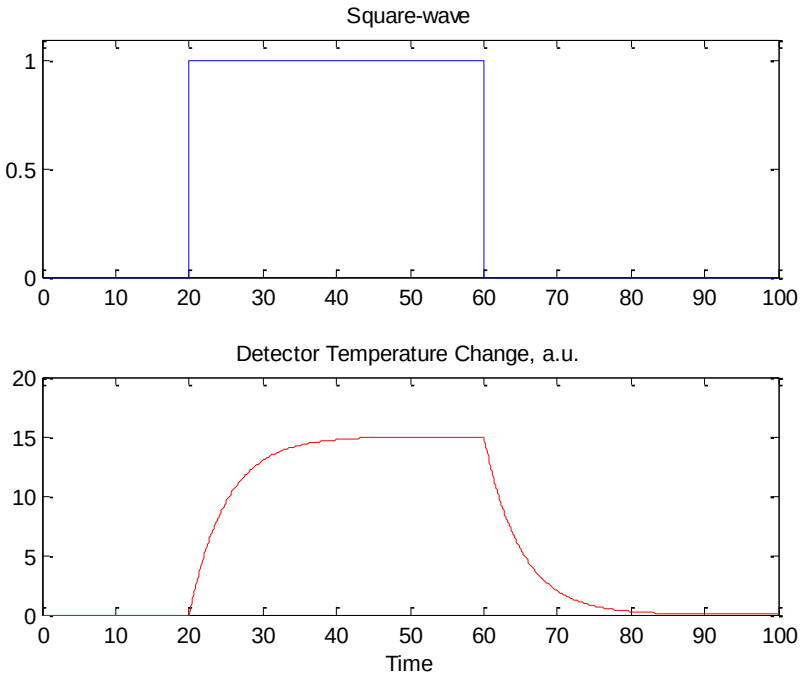

Figure 1.4: Thermal detector response to incident square-wave pulse of thermal radiation

1.6 Photon detectors

Photon detectors operate by measuring the absorption of photons through direct conversion to electrical current. This absorption causes a change in carrier density and is referred to as the internal photoelectric effect. Semiconductors generally have electron energy bands and energy gaps. The energy gaps are forbidden energy levels where the electrons may not reside. The amount of energy needed for an electron to be excited into the conduction band from the valence band is known as the band gap energy (E_g). Band gap energies for common semiconductors are found in Table 1-1. Figure 1.5 shows a basic energy level diagram of a general semiconductor. The band gap energies may be changed by the introduction of impurities (dopants) which introduce energy bands where electrons may reside.

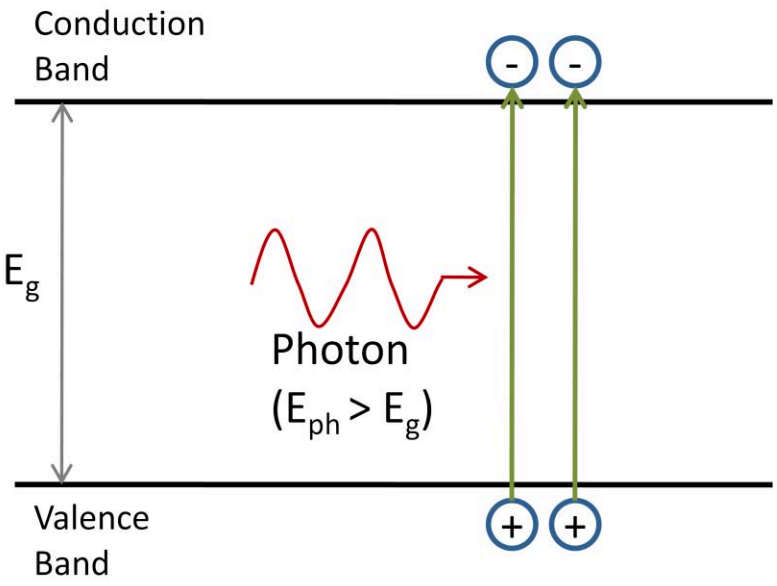

Figure 1.5: Energy band diagram of a general semiconductor showing the electron hole pair generation due to an incident photon

Material	Bandgap Energy (eV)
Silicon (Si)	1.12
Gallium Arsenide (GaAs)	1.42
Germanium (Ge)	0.66
Indium Phosphide (InP)	1.35

Table 1-1: Common Semiconductor Bandgap Energies [10, 11]

Due to the nature of the band gap energy there exists an ideal cutoff wavelength or frequency of detection. Photons have an energy described by Equation 1-7 where h is Plank's constant (6.626×10^{-34} J·s) and v is the photon frequency or by Equation 1-8 where c is the speed of light and λ is the photon wavelength.

Equation 1-7 $$E_{photon} = hv$$

Equation 1-8 $$E_{photon} = hc/\lambda$$

The minimum detectable photon wavelength is calculated by inserting the band gap energy into Equation 1-7 and solving for the frequency or wavelength. This relation is described in Equation 1-9 for cutoff frequency and Equation 1-10 for cutoff wavelength.

Equation 1-9 $$v_{cutoff} = E_g/h \text{ (Hz)}$$

Equation 1-10 $$\lambda_{cutoff} = \frac{ch}{E_g}(m)$$

The detector is only sensitive to light with frequencies larger than the cutoff frequency. For IR detection a smaller bandgap is needed because of the lower photon energies. For example, in an ideal case a 5µm detector must have $E_g \leq 248\ meV$. To estimate the probability of thermal noise excitation we can assume $E_g \leq 3k_BT$ and therefore use the simplified Boltzmann equation where T is the temperature and k_B is the Boltzmann constant (8.614×10^{-5} eV/K) (Equation 1-11) [10].

Equation 1-11 $$\mathcal{P}(T) = e^{-\frac{E_g}{k_BT}}$$

At room temperature (T = 300K) the exponential of the probability of thermal noise excitation is 6.94×10^{-5}. When the system is cooled down to liquid nitrogen temperatures (T = 77 K) the exponential becomes 5.68×10^{-17}. The exponential of the simplified Boltzmann equation is reduced by 12 orders of magnitude. The cooling of the detector greatly reduces the free carrier concentration due to ambient thermal excitement therefore reducing thermal noise. As the cutoff wavelength increases so does the need for cooling of the detector. For example assuming the same ideal photon detector for a 10 µm cutoff wavelength the exponential of the Boltzmann model becomes 8.3×10^{-3} for room temperature and 7.6×10^{-9} for liquid nitrogen temperature.

Almost all 8 – 14 µm photon detectors operate at 77 K by liquid nitrogen cooling, the 3 – 5 µm range is either cooled to 77 K or thermoelectrically cooled to around 200 K, and the 0.9 – 1.7 µm range is thermoelectrically cooled to 200 K [2]. Cooling apparatuses use space and increase cost. It would be most efficient to have detection in the LWIR region without the use of cooling; for this situation thermal detectors can have advantages as they do not suffer from thermal carrier excitations.

1.7 Detector Metrics

The figure of merit for thermal detectors is the specific spectral detectivity (D_λ) allowing different types of detectors to be compared. To calculate D_λ the responsivity and noise equivalent power must be known. The responsivity is the ratio of the output signal to the incident radiant power (Equation 1-12).

Equation 1-12
$$\mathcal{R} = \frac{V_{signal}}{P_{radiation}} \left(\frac{V}{W}\right)$$

After calculating the responsivity the noise equivalent power (NEP) can solved for. NEP is the ratio of the detector noise to the responsivity (Equation 1-13).

Equation 1-13
$$NEP = \frac{V_{noise}}{\mathcal{R}} = \frac{V_{noise} P_{radiation}}{V_{signal}} \left(\frac{W}{\sqrt{Hz}}\right)$$

The NEP value gives the required power for a signal to noise ratio of unity. Specific detectivity is calculated as the ratio of the square root of the detection area to NEP. Equation 1-14 shows the detectivity where A_D is the detection area.

Equation 1-14

$$D_\lambda = \frac{\sqrt{A_D}}{NEP}\left(\frac{cm\sqrt{Hz}}{W}\right)$$

The knowledge of the detectivity gives a reasonable estimate for NEP of given detector geometries and the bandwidth of signal detection.

1.8 Thermal Detectors

Current commercial thermal detectors are slow and their sensitivity can be improved. The most lucrative thermal detectors, microbolometers, are constructed with a silicon nitride and vanadium oxide layer supported by at least two metallic arms, the silicon nitride absorbs radiation and heats the vanadium oxide causing a change in resistance. Underneath the absorbing layer a high reflectance material is placed to create a cavity helping total absorption. The measured change in resistance of the vanadium oxide is processed as the photoresponse. The highest performance bolometers have rise times in the range of 10 – 40 ms and specific detectivities around 4×10^8 $\frac{cm\sqrt{Hz}}{W}$; almost 2 orders of magnitude worse than the ideal case of 1.8×10^{10} $\frac{cm\sqrt{Hz}}{W}$ which neglects Johnson-noise [2, 12, 13]. Improvements to speed and sensitivity are the most desirable. Figure 1.6 shows the detectivities for various infrared detectors; note the difference of ideal detection and the commercially available bolometer as well as the depleting performance of photon detectors in the LWIR region.

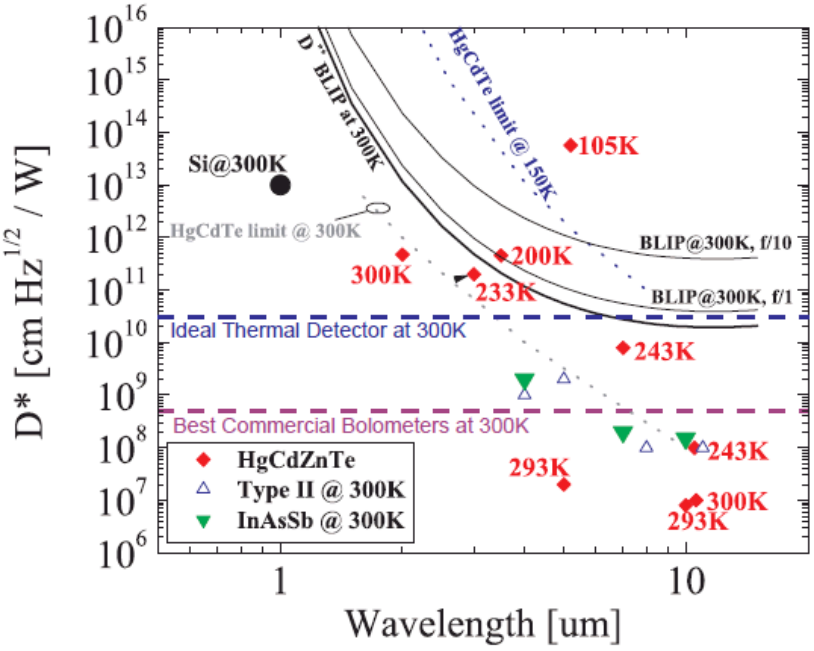

Figure 1.6: Comparison of detectivities for various infrared detectors [14]

1.9 THZ Imaging

THz radiation can pass through some common objects, such as clothing and has interesting security applications. Unlike x-rays, THz radiation is non-ionizing due to its low photon energy, potentially providing a safer alternative to x-ray imaging. THz imaging can also be used in chemical detection as many compounds have unique THz fingerprints. Figure 1.7 (a) shows an image of a packaged semiconductor device. The THz radiation passes through the plastic packaging but not through the metallic leads. Figure 1.7 (b) shows images of a leaf directly after being cut and 48 hours later. The THz radiation is absorbed by the water in the leaf therefore allowing the loss of water to be characterized. These are just two examples demonstrating some unique scenarios where THz imaging can have advantages over other approaches.

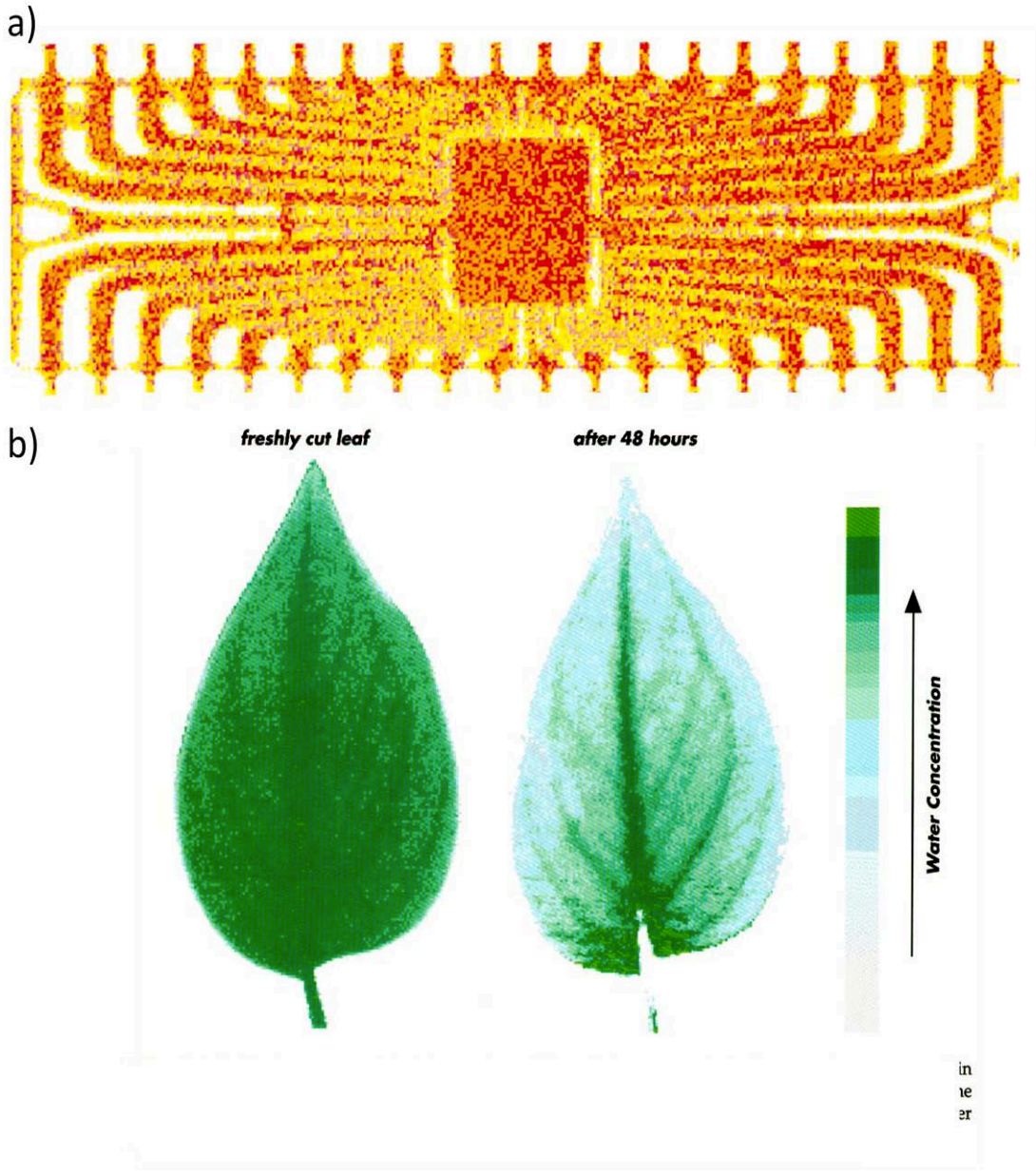

Figure 1.7: a) THz image of a packaged integrated circuit b) THz image of a freshly cut leaf compared to itself 48 hours later revealing the loss in water content [1]

1.10 Applications

Due to the extreme precision of modern thermal imaging, slight changes in body temperature can be observed. It is well known that injuries as well as diseases lead to changes in body temperature, for example swelling. In the medical field physicians are mostly interested in internal processes leading to abnormal blood flow. Abnormal blood flow causes an asymmetric heating of a body part. Figure 1.8 is a thermal image taken of an unconscious subject. Due to the unconscious state the subject was unable to assist in providing information about the injury. A thermal image was taken of the subject revealing an abnormality in the abdominal area which later was found to be cause by a fractured rib [6].

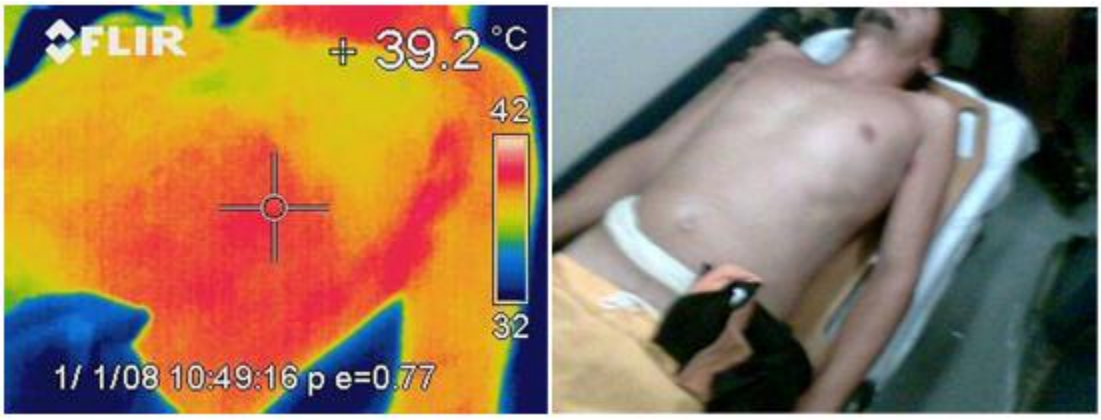

Figure 1.8: Image shows abnormal body heating due to rib fracture [6]

In many industrial settings heat flow/control is an important in the operation of certain mechanisms. For instance in a nuclear facility many mechanical parts heat due to the energy conversion process. The flow of heat away from these parts is important in the performance of the system. Figure 1.9 shows a heat management metal piece that is not working correctly due to a loose bolt, after tightening the management structure

began to work properly. Thermal imaging was able to locate the problem before serious malfunction occurred.

Figure 1.9: Thermal image of heat management equipment taken in a power plant [5]

Chapter 1 References

[1] B. B. Hu and M. C. Nuss, "Imaging with Terahertz Waves," *Optics Letters,* vol. 20, pp. 1716-&, 1995.

[2] M. Vollmer and K.-P. Mollmann, *Infrared Thermal Imaging*: Wiley-VHC, 2010.

[3] K. Agarwal*, et al.*, "Thermal imaging in healthy humans, what is not normal skin temperature?," in *Inframation 2007*, 2007.

[4] D. L. Harper, "The value fo infrared thermography in the diagnosis and prognosis of injuries in animals," in *Inframation 2000*, 2000.

[5] M. J. Ralph, "The continuing story of power plant thermography," in *Inframation*, 2009.

[6] M. L. Brioschi, "Infrared imaging for emergeny medical services (EMS): Using an IR camera to identify life-threatening emergencies," in *Inframation*, 2008.

[7] http://mivim.gel.ulaval.ca.

[8] M. Planck, "On the Law of Distribution of Energy in the Normal Spectrum," *Annalen der Physik,* 1901.

[9] http://www.astro.virginia.edu.

[10] D. A. Neaman, *Semiconductor Physics and Devices*: Elizabeth A. Jones, 2005.

[11] J.-M. Liu, *Photonic Devices*: Cambridge University Press, 2005.

[12] P. L. Richards, "BOLOMETERS FOR INFRARED AND MILLIMETER WAVES," *Journal of Applied Physics,* vol. 76, pp. 1-24, Jul 1994.

[13] J. C. Mather, "BOLOMETER NOISE - NON-EQUILIBRIUM THEORY," *Applied Optics,* vol. 21, pp. 1125-1129, 1982.

[14] M. R. Watts*, et al.*, "Thermal Microphotonic Focal Plane Array (TM-FPA)," Sandia National Laboratories, Albuqueruqe 2009.

Chapter 2 Silicon Photonics

In this chapter the design and fabrication of the microphotonic thermal detector is presented. For future imaging applications (large scale integration) it is important to design the microphotonic detector to be compatible with CMOS fabrication processes. The fabrication process as well as the reasoning for the selection of materials will be shown.

2.1 Infrared Detection using Silicon Photonics

The high quality factors (Q) of optical microring resonators have enabled the design and demonstration of highly sensitive microring-resonator-based sensors. Examples include chemical, biological, nuclear, inertial, and thermal sensors [1-5]. In the case of a thermal detector, a temperature change in the resonator will induce a change in the index of refraction (n) of the ring or disk causing a change in the resonance wavelength. The change in resonance is measured by a change in the transmission of a bus waveguide

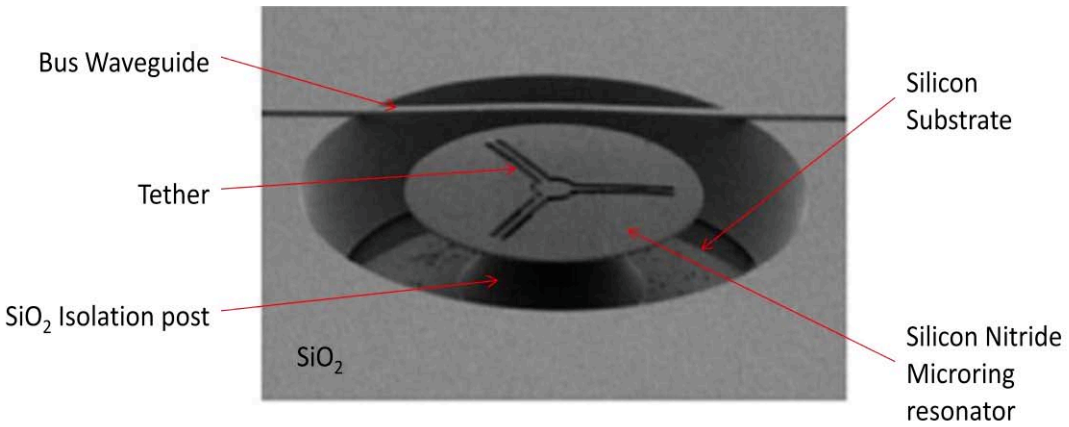

Figure 2.1: Schematic of microphotonic thermal detector showing the silicon substrate, bus waveguide, microdisk resonator, tethers, and silicon dioxide isolating post

w

which is measured using an optical detector. The microphotonic thermal detector is shown in Figure 2.1, which displays the important components such as the absorber, bus waveguide, isolating tethers, and insulating post. The insulating post and tethers isolate the microring from the substrate thereby reducing the thermal flux (noise) from the microdisk to the substrate which acts as a heat sink. The thermal noise, also known as phonon noise, is expressed by Equation 2-1 in terms of NEP [6]. Physically this noise arises from the passage of quantized carriers of energy through the thermal linkage; this movement causes white noise (frequency independent noise) [7].

Equation 2-1 $$NEP_{phonon} = \sqrt{4k_B G}T \ (W/\sqrt{Hz})$$

In the case of the microphotonic thermal detector, G is the thermal conductance through the insulating post and isolating tethers to the substrate, k_B is the Boltzmann constant, and T is temperature expressed in Kelvin. The noise floor of the detector does not include any Johnson-noise; this is due to the absence of electronic measurement. The elimination of the Johnson-noise increases the potential overall noise performance of microphotonic detector giving it an edge over current commercially available thermal detectors. The microphotonic detector was designed to operate at room temperature to detect LWIR radiation, whereas photon detectors in this region must be cooled to do so. Hand calculations produce a thermal conductance of G = 1.4×10^{-7} W/K which is limited by the silicon nitride tethers.

2.2 Waveguide Construction

The bus waveguide serves as a medium for interrogation light to propagate for inspection of the microdisk by evanescent coupling, which occurs when the waveguide and disk are close enough in proximity for the evanescent fields in the waveguide to excite whispering-gallery-modes in the disk [5]. These fields are described by solving Maxwell's equations for a square waveguide with dimensions depicted in Figure 2.2. Using the separation of variables method, Equation 2-2, the Helmholtz equation can be solved. The Helmholtz equation for the square waveguide with lossless and source free medium is described in Equation 2-3.

Equation 2-2 $$E(x,y,z) = f(x)g(y)h(z)$$

Equation 2-3 $$\nabla^2 E + \beta^2 E = 0$$

The solutions are found to be standing waves in the core region of the waveguide and evanescent waves in the cladding region. The standing waves are described by sine and cosine functions (Equation 2-4) and the evanescent waves are described by decaying exponentials (Equation 2-5). A more in depth solution and helpful table can be found on pg. 110 in reference [8].

Equation 2-4 $$f_{core}(x) = A\cos(\beta_{core}x) + B\sin(\beta_{core}x)$$

Equation 2-5 $$f_{cladding}(x) = Ce^{-\gamma x} + De^{\gamma x}$$

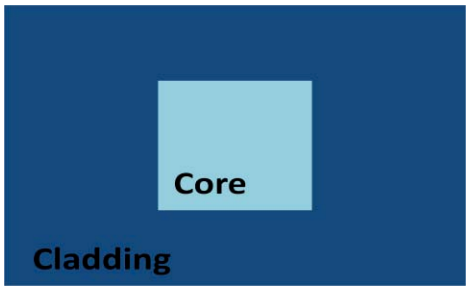

Figure 2.2: Basic layout of square dielectric waveguide, $n_{core} > n_{cladding}$

2.3 Planar Ring Resonators

Evanescent microring waveguide sensors have been studied extensively over the past years showing that whispering-gallery-modes are prevalent in microring technology leading to the obtainable high quality factors. The schematic of an evanescently coupled planar ring resonator is depicted in Figure 2.3. The resonant wavelength is given in Equation 2-6, where n_{eff} is the effective refractive index of the ring, r is the radius of the ring, and N is an integer [5].

Equation 2-6

$$\lambda_{res} = \frac{2 \cdot \pi \cdot r \cdot n_{eff}}{N}$$

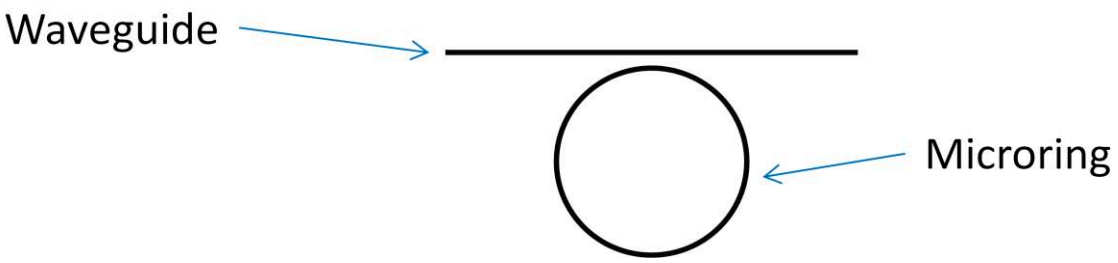

Figure 2.3: Microring resonator and waveguide for interrogation light

The interrogation light in the bus waveguide is intended to measure a shift in resonance which is directly related to a change in the resonance of the ring. The shift is caused by a

change in the effective refractive index, related by Equation 2-7 where FSR is the free spectral range of the ring and λ_o is the resonance wavelength [5].

Equation 2-7 $$\Delta\lambda = \frac{\Delta n_{eff} \cdot FSR \cdot \pi \cdot r}{\lambda_o}$$

The change in resonance will change the transmission of the interrogation light; ultimately the change in transmission will lead to a change in power received by a photodetector which transduces the relative intensity shift into an electrical signal (Further discussion in chapter 3).

2.4 Quality Factor

The responsivity resolution of these devices is characterized by the quality factor (Q). The quality factor is expressed in Equation 2-8 where ω_O is the resonance wavelength and ω_{FWHM} is the full width at half maximum of the resonance.

Equation 2-8 $$Q = \frac{\omega_O}{\omega_{FWHM}}$$

2.5 Materials chosen

For large scale imaging applications it was important to design the microphotonic detector to be compatible to a CMOS fabrication process because of the large infrastructure currently existing in industry, ability for large scale integration, lower costs, and high yields. Due to the spectrum of a blackbody, as discussed in chapter 1, the wavelengths of interest to detect reside in the LWIR region, 8 – 14 µm. Silicon nitride is a desirable material because it provides good absorption in this wavelength range, is transparent at 1.55µm, can be implemented into a fabrication process, and has small

nonlinearities [9]. The only setback of silicon nitride is its low refractive index which leads to the necessity of a larger diameter microdisk because of bending losses at the lower index. Figure 2.4 shows a plot of the index of refraction and extinction coefficient taken by J. A. Woollam Co., Inc. using IR-VASE® ellipsometer [9]. The measured data shows that in the 9 – 12 µm range silicon nitride possesses an increase in absorption as well as transparency in the 1 – 3 µm range giving good reason to use silicon nitride as the bus waveguide as well as the radiation absorbing layer. Therefore Silicon nitride makes for a good deposited layer with efficient optical characteristics for a simple process flow.

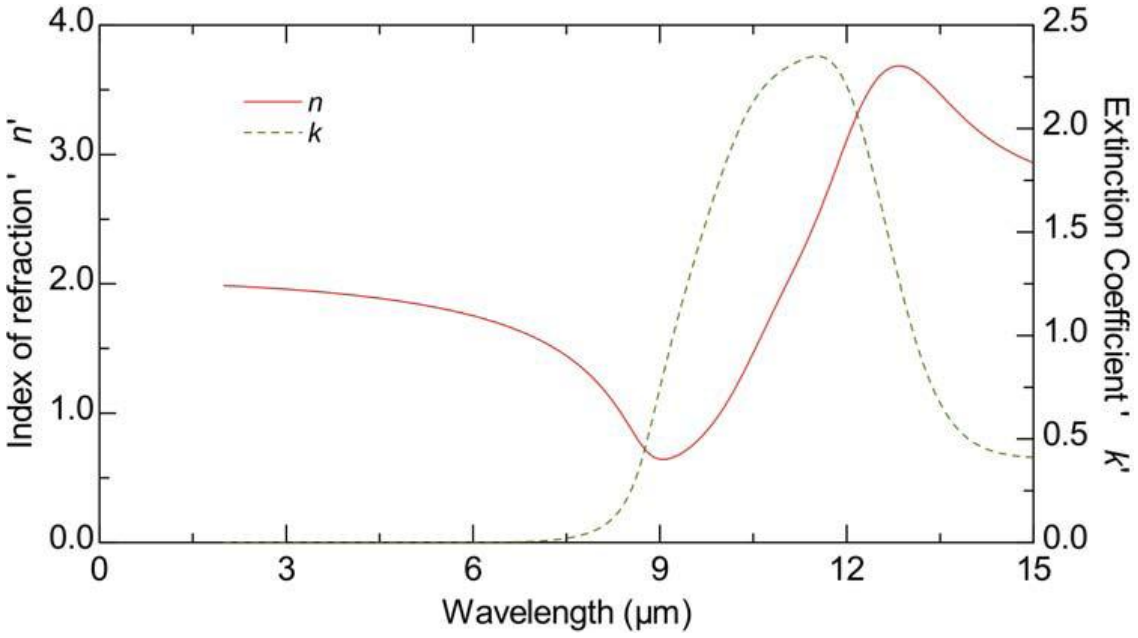

Figure 2.4: Plot of optical constants for silicon nitride material used in the microphotonic detector showing good extinction at wavelengths between 9 and 13µm. The data was measured be J. A. Woollam Co., Inc. with an IR-VASE® ellipsometer [9]

2.6 Fabrication Process

The microphotonic detectors were produced at the Microelectronics Development Lab (MDL) at Sandia National Laboratories (SNL). A top down approach on a silicon wafer with a 10 μm silicon dioxide layer was used. A 200nm thick silicon nitride layer by means of low-pressure chemical vapor deposition (LPCVD) is deposited on the silicon dioxide. High temperature processes have proven most successful in low loss optical properties of silicon nitride. Both stoichiometric silicon nitride and low stress silicon nitride have been investigated for use of waveguide systems; stoichiometric silicon nitride has proven to be the better choice due to limitations of the photo resist thickness, reactive ion etch capability, and material losses [9]. The bus waveguide and microdisk are patterned from silicon nitride. The small dimensions of these devices, mainly due to the thermal isolating tethers, require the use of an ASML scanner stepper with a minimum resolution capability of 150 nm, and a maximum photo resist thickness of 1.3 μm. To further help thermal isolation the silicon dioxide layer underneath the microdisk was removed with a hydrofluoric (HF) wet etch. A polysilicon layer was used as the hard mask and etched around the ring to allow for the isotropic HF wet etch. The unit is then placed in another isotropic wet etch to remove the polysilicon. The resultant is the microphotonic thermal detector. Figure 2.5 shows the process flow of the fabrication of the IR microphotonic detector. Figure 2.6 shows the resultant microring resonator for thermal detection.

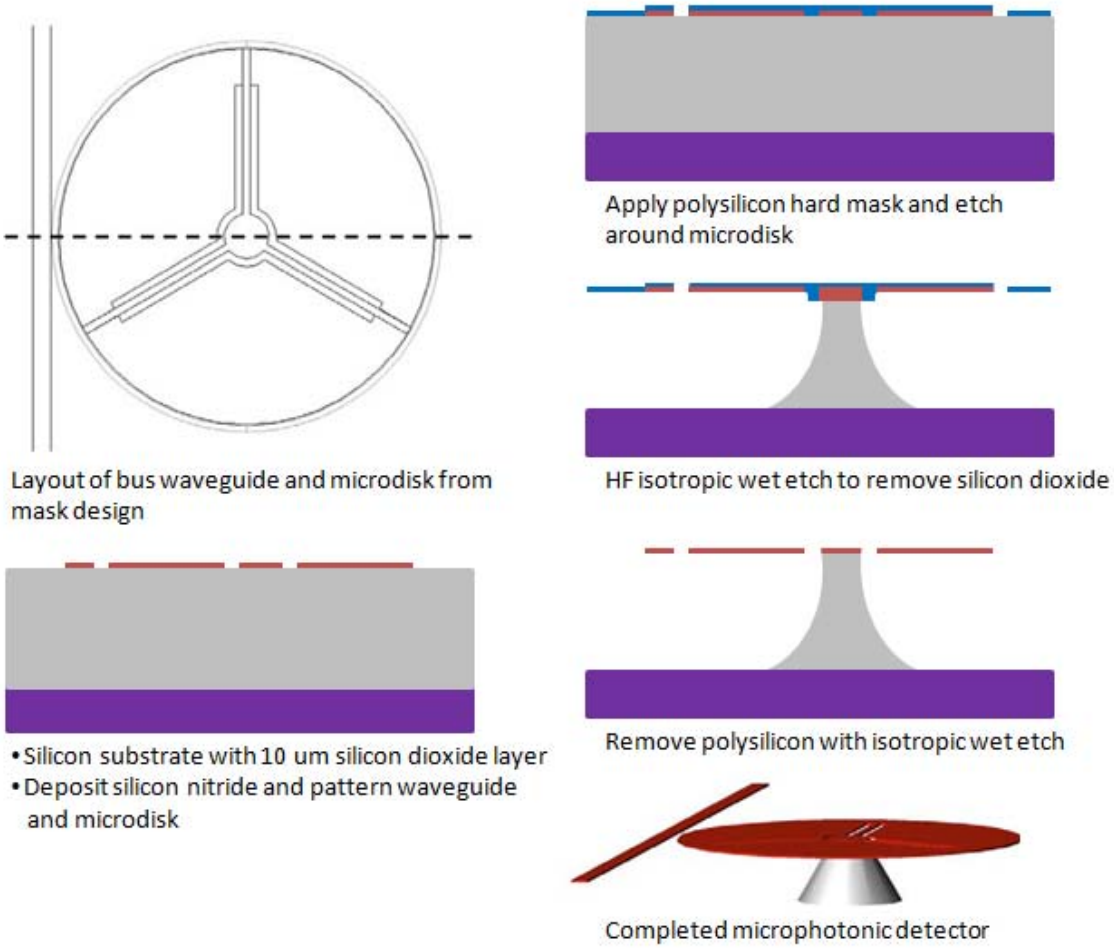

Figure 2.5: Process flow of microphotonic thermal detector [9]

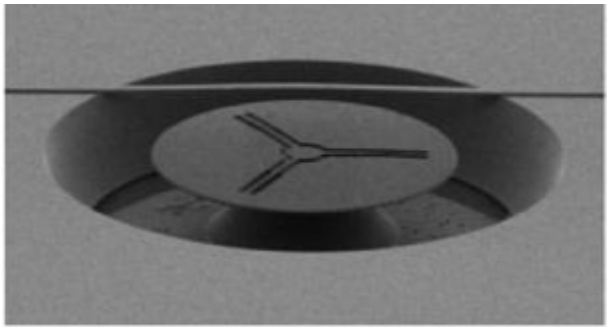

Figure 2.6: Image of Microring resonator for thermal detection

Chapter 2 References

[1] A. Densmore*, et al.*, "Sensitive label-free biomolecular detection using thin silicon waveguides," *Advances in Optical Technologies,* p. 725967 (9 pp.), 2008.

[2] D. Xu*, et al.*, "Silicon photonic wire devices for biosensing and communications," *2010 Asia Communications and Photonics Conference and Exhibition (ACP 2010),* p. 52, 2010.

[3] M. R. Watts*, et al.*, "Optical resonators - Microphotonic thermal imaging," *Nature Photonics,* vol. 1, pp. 632-634, Nov 2007.

[4] K. Suzuki*, et al.*, "Monolithically integrated resonator microoptic gyro on silica planar lightwave circuit," *Journal of Lightwave Technology,* vol. 18, pp. 66-72, 2000.

[5] J. Wright, "High Quality Factor Silicon Nitride Ring Resonators for Biological Sensing," M.S., Electrical Engineering, University of New Mexico, Albuquerque 2010.

[6] J. C. Mather, "BOLOMETER NOISE - NON-EQUILIBRIUM THEORY," *Applied Optics,* vol. 21, pp. 1125-1129, 1982.

[7] P. L. Richards, "BOLOMETERS FOR INFRARED AND MILLIMETER WAVES," *Journal of Applied Physics,* vol. 76, pp. 1-24, Jul 1994.

[8] C. Balanis, *Advanced Engineering Electromagnetics*: John Wiley & Sons, Inc, 1989.

[9] M. R. Watts*, et al.*, "Thermal Microphotonic Focal Plane Array (TM-FPA)," Sandia National Laboratories, Albuqueruqe 2009.

Chapter 3 Microphotonic Thermal Detection Results

To be competitive the microphotonic thermal detector must be comparable to commercial thermal detectors. This chapter will present the characterization of the microphotonic thermal detector showing, that in early design stages, the microphotonic detector surpasses the performance of the microbolometer in size, speed, and noise. The detectivity of these two technologies is currently comparable, but with minor design modifications the detectivity of the microphotonic detector should increase by an order of magnitude, thus, surpassing the microbolometer.

3.1 Measurement Setup

A custom designed vacuum chamber was used for the testing of the microphotonic thermal detector. The vacuum apparatus consists of ports for optical fibers, electronics, pumping, and a window for thermal interrogation (Figure 3.1). The chamber contains an optical bread board, two electrically driven 3-axis stages, a pair of lensed fibers, a thermoelectric cooler, and a one-axis stage for sample mounting. During measurements the chamber is evacuated to pressures in the 10^{-5} Torr range to improve the thermal resistance of the disk resonator from the substrate. The optical feed-throughs are used for the input of the interrogation laser to be coupled to the bus waveguide using the lensed fibers. Alignment of the lensed fibers is done using the 3-axis stages. The electrical feed-through is for the wiring of the multiple stage motors and the thermoelectric cooler. The window of the apparatus is made of KRS-5 (Thallium Bromo-Iodide) with a measured transmission of $T_{window} = 0.7$; this was measured using a

NIST calibrated pyroelectric detector to compare the incident radiation to the transmitted radiation of the window. A CO_2 laser operating at 10.6 µm was used for the characterization of the microphotonic detector. The CO_2 laser was internally chopped, referenced by a TTL signal producing a square-wave modulated output. Before interrogation of the microphotonic detector the power of the laser must be attenuated. This was done using a 99% reflection optic and a wire-grid polarizer pair. The CO_2 beam is brought into the vacuum chamber perpendicularly by an optical mirror mounted to a microscope head. The beam is purposely not focused to promote flood illumination of the resonator.

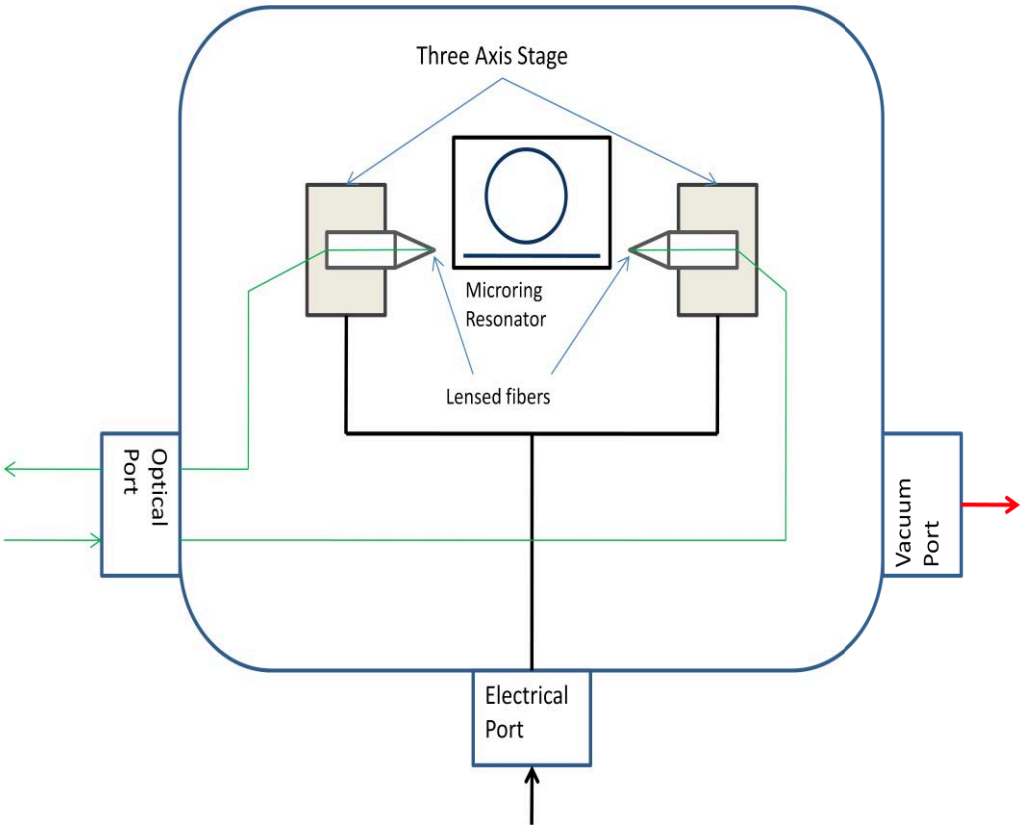

Figure 3.1: Schematic of the vacuum assembly showing optical, electrical, and vacuum ports as well as the three axis stages, lensed fibers, and microphotonic detector

3.2 Bus Waveguide Transmission

The first step in characterizing the microphotonic detector was to measure the transmission of the bus waveguide to locate the resonance wavelengths. Figure 3.2 shows a plot of the bus waveguide transmission showing multiple resonance wavelengths. The FSR of the microphotonic detector was found to be $FSR = 23\,nm$. The 1557 nm resonance wavelength was chosen for characterization of the microphotonic detector, Figure 3.4 shows an enlarged view of this resonance. For characterization, the bus waveguide interrogation laser must set at the 3 dB point of the resonance. As shown in Equation 2-7, a change in the effective index of the microdisk changes the resonance wavelength causing a change in transmission of the bus waveguide. The effective index of the microdisk will change as its temperature changes. A measured change in transmission is processed as a sensed temperature change.

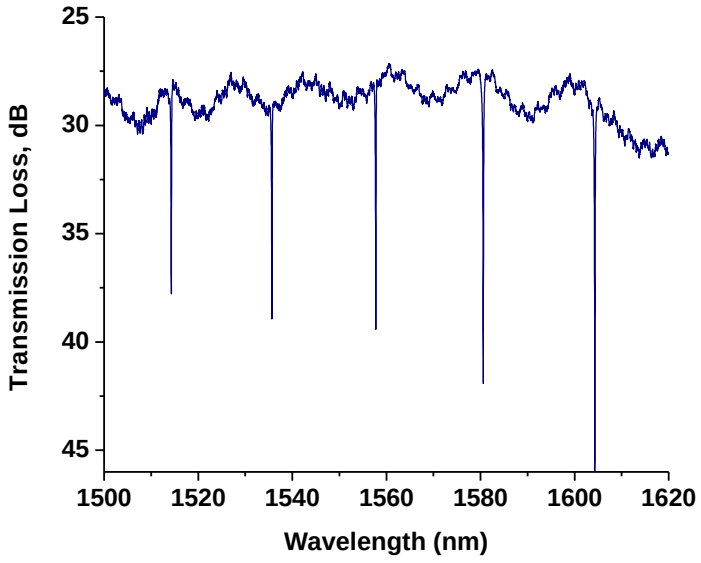

Figure 3.2: Transmission of the bus waveguide showing the multiple resonance wavelengths of the microphotonic thermal detector.

3.3 Incident Power Calculation

The $C0_2$ illumination leads to heating of the microphotonic detector and therefore a change in resonance frequency. To measure the sensitivity of the resonator the incident CO_2 power on the disk must be known. To do so a beam profile (Figure 3.3) and power measurement were done, beam profiles were taken at the detector location using a Spiricon Pyrocam III. It can be seen in the Pyrocam image that the measured beam has a Gaussian profile with a diameter of 8.93 mm with a full width half maximum (FWHM) of 6.25 mm. The measured total incident power onto the window was 3.71 mW. Using a Gaussian approximation (Equation 3-1) the incident power on the disk was calculated.

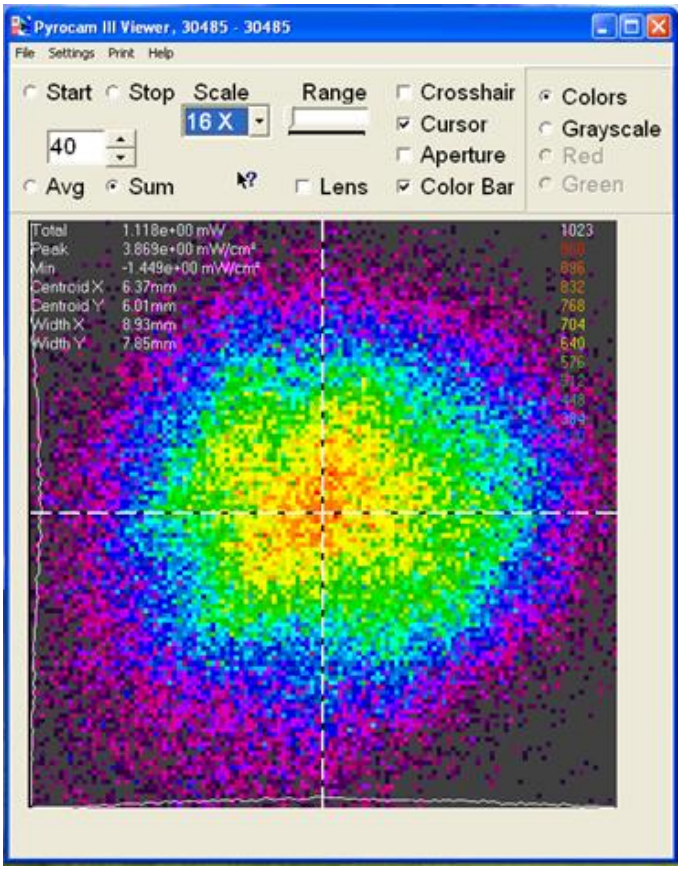

Figure 3.3: Image of $C0_2$ beam taken with the Spiricon Pyrocam III. The FWHM of the beam is 6.25 mm.

Equation 3-1

$$I(\rho) = A\exp\left(-\frac{\rho^2}{2c^2}\right)$$

Equation 3-2

$$c = FWHM/\sqrt{8\ln 2}$$

Solving Equation 3-2 we find $c = 2.7mm$. To solve for the coefficient A, integration of the Gaussian function over the range of $\rho[0,\infty)$ and $\theta[0,2\pi]$ was performed.

Equation 3-3

$$P_{total} = \iint_{0\,0}^{2\pi\,\infty} A\exp\left(-\frac{\rho^2}{2c^2}\right)\rho d\rho d\theta = 2\pi A 2c^2(1 - 0) = 4\pi c^2 A$$

Solving for Equation 3-3 we find A = 45.29mW/m^2. To solve for the incident power on the disk Integration is again performed on equation 3-1 over the range $\rho[0,10\mu m], \theta[0,2\pi]$. The solution of the integral is the incident power of a $20\,\mu m$ diameter disk centered in the Gaussian beam incident on the window of the chamber, $P' = 267.6\,pW$. Finally, to solve for the incident power on the microdisk, P' is multiplied by the transmission of the window ($P_D = P'T_{window}$). The incident power on the disc was found to be $P_D = 184.5pW$.

3.4 Characterization

As discussed earlier the interrogation laser wavelength must rest on the 3dB point of the resonance. Figure 1.1Figure 3.4 shows the chosen resonance for characterization. Using Equation 2-8 the Q of the 1557 resonance was calculated as 1.5 × 10^4. The 3 dB alignment may be achieved in two different ways: (1) by thermally changing the resonance of the disc by means of the thermoelectric cooler or (2) by changing the wavelength of the laser. Either way the thermoelectric cooler must be used to ensure

that large temperature fluctuations do not occur as this would change the resonance wavelength and therefore the signal. The chosen method was to thermoelectrically stabilize the temperature while supplying an adjustable wavelength interrogation laser. The transmitted power through the bus waveguide was measured with the New Focus 2053 InGaAs photoreceiver. The output of the photoreceiver was evaluated in either the SR785 Lock-in-amplifier or the SR850 spectrum analyzer. Generally the Lock-in-amplifier was used during the $C0_2$ alignment due of the ability for low integration times and to lock-in on the chopping frequency. The spectrum analyzer was used to measure the spectrum of the system for noise analysis. Figure 3.5 shows a spectrum of the resonator given by the SR785 spectrum analyzer.

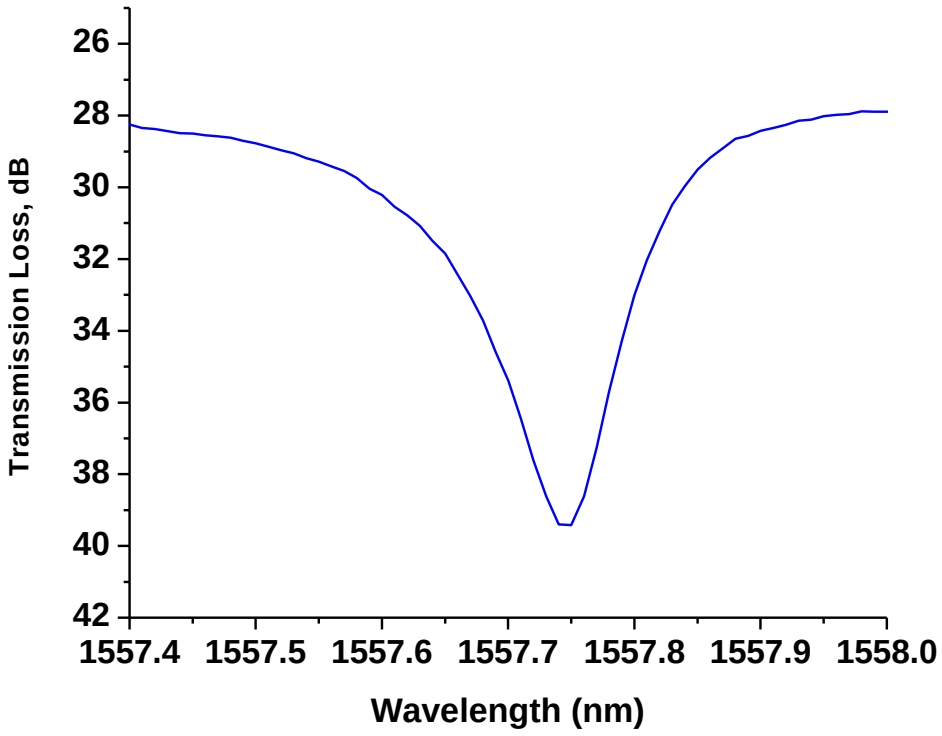

Figure 3.4: 1557 nm resonance of microphotonic thermal detector, Q ≈ 15000.

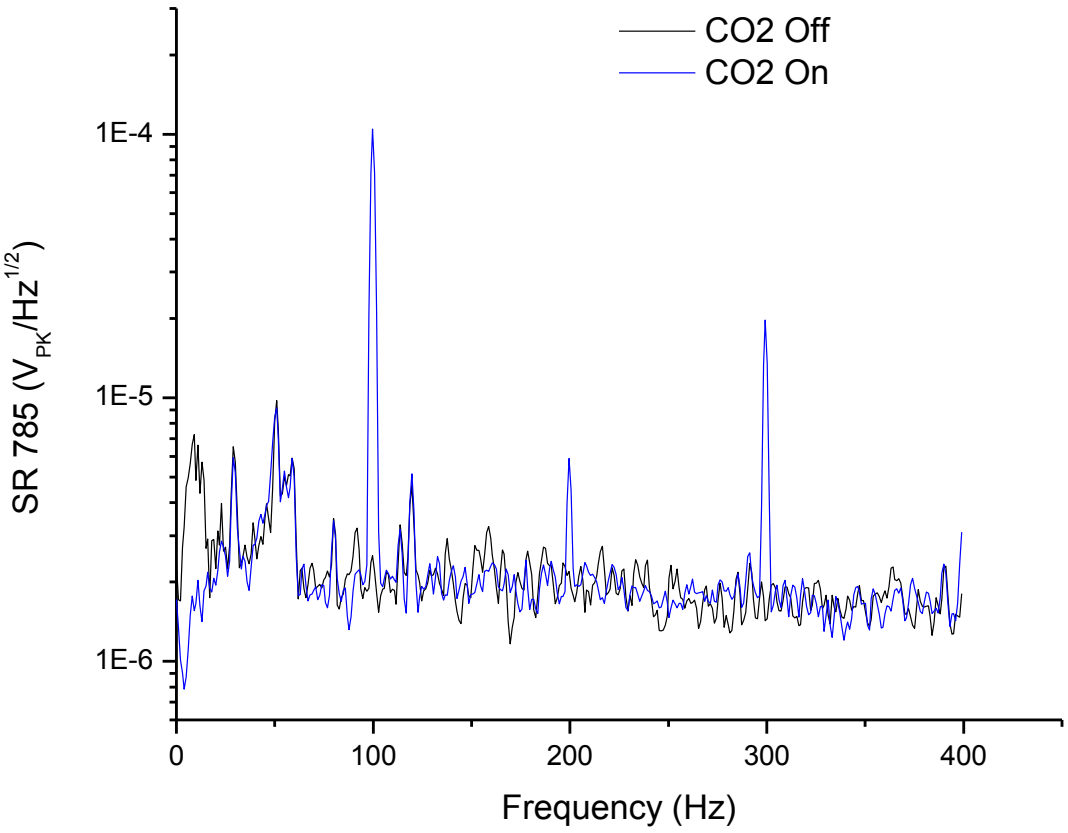

Figure 3.5: Spectral plot of microphotonic thermal detector with incident 100 Hz square-wave modulated radiation

3.5 Characteristic Calculations

As discussed in chapter 1 the important characterizations of thermal detectors are thermal time constant (τ), responsivity ($\mathcal{R}$), noise equivalent power (NEP), and specific spectral detectivity ($\mathcal{D}_\lambda$). The signal voltage of the detector was measured using the SR785 spectrum analyzer and found to be $V_{Signal} = 109.477\mu V$. The SR785 references the input signal to a sine-wave; therefore the square-wave input into the SR785 is broken into separate sinusoidal harmonics. Equation 3-4 shows the Fourier series of the square-wave where n is the harmonic.

Equation 3-4

$$a(t) = \frac{4}{\pi}\sum_{n=1}^{\infty}\frac{1}{n}\sin 2n\pi ft$$

Due to this de-convolution the first harmonic of the $C0_2$ power must be calculated. The power of the first harmonic is given by Equation 3-5 where the transfer function of the square-wave is $F(\omega_1) = \frac{1}{1+j\omega\tau}$.

Equation 3-5

$$P_1 = \frac{P_{Disc}|F(\omega_1)|}{\sum_{n=1}^{\infty}\frac{1}{n}|F(\omega_n)|}$$

For a chopping frequency of 100 Hz the power of the first harmonic is calculated to be $P_1 = 97.84\ pW$ and therefore responsivity is calculated to be $\mathcal{R} = 1.12\ \times 10^6 V/W$.

3.6 NEP and Detectivity Calculation

Noise equivalent power (NEP) is a calculation to determine the minimal amount of signal detectable, in other words where the signal-to-noise ratio is unity. The noise of the detector system was measured using the SR850. With the $C0_2$ beam blocked the noise was found to be $N = 8\ \mu V/\sqrt{Hz}$ at 100Hz. As a result the NEP of the system was calculated to be $NEP = 7.15\ \times 10^{-12}\ W/\sqrt{Hz}$. This NEP is better than commercial detectors by almost an order of magnitude. Although the NEP is a good basis, the figure of merit is the specific spectral detectivity. The area of the microphotonic detector is $\pi\ \times\ 10^{-6}\ \mathrm{cm}^2$ resulting in a calculated specific detectivity of $\mathcal{D}_\lambda = 2.47\ \times\ 10^8\ \frac{cm\sqrt{Hz}}{W}$; the detectivity is on the order of the best commercial thermal detectors ($\mathcal{D}_\lambda^{comm} = 4\ \times\ 10^8\ \frac{cm\sqrt{Hz}}{W}$). Bolometer design has taken many years whereas the

microphotonic thermal detector is relatively new, showing great potential for future development.

3.7 Thermal Time Constant

The thermal time constant is a measure of the speed of a thermal detector. Figure 3.6 shows the temporal response of the microphotonic detector to a square-wave modulated thermal radiation source. The thermal time constant can be found by measuring the amount of time it takes for the microphotonic detector to reach a normalized value of $1 - {}^{1}/_{e} \approx 0.632$. The time constant was found to be 2 ms, a fraction of the best commercially available high sensitivity thermal detectors which range from 10 – 40 ms [2,3]. Although the microphotonic detector has a lesser detectivity than microbolometers, its thermal time constant is much faster making it potentially more useful in high speed applications.

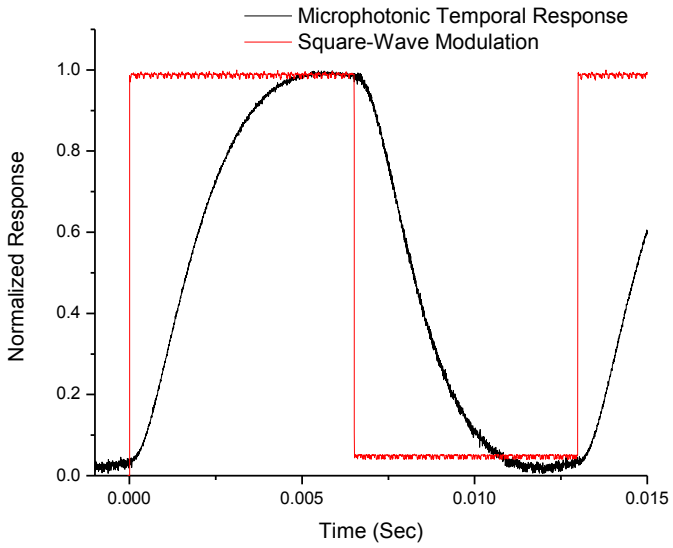

Figure 3.6: Temporal response of microphotonic detector to incident square-wave radiation

3.8 Design Improvements

Current commercial detectors have high reflectance material underneath the absorber improving overall absorption. For better detection, a high reflectance material could be placed in the design of the microphotonic detector to create a cavity effect. The increased difficulty of the fabrication process is outweighed by the overall gain in absorption. Figure 3.7 shows simulation results for absorption at different substrate to resonator spacing. Currently the spacing between the disc and substrate is about 10 μm which was found through the simulation to have an absorption of only 7.5%. For maximum detection, it would be best to have a spacing of λ/4 or 3 λ /4. The relatively low quality factor, Q = 15000, could be increased to obtain a higher responsivity, although the quality factor will not change internal NEP due to thermal fluctuation a smaller FWHM of the resonance would allow for a greater number of resonators to be placed on a single bus waveguide.

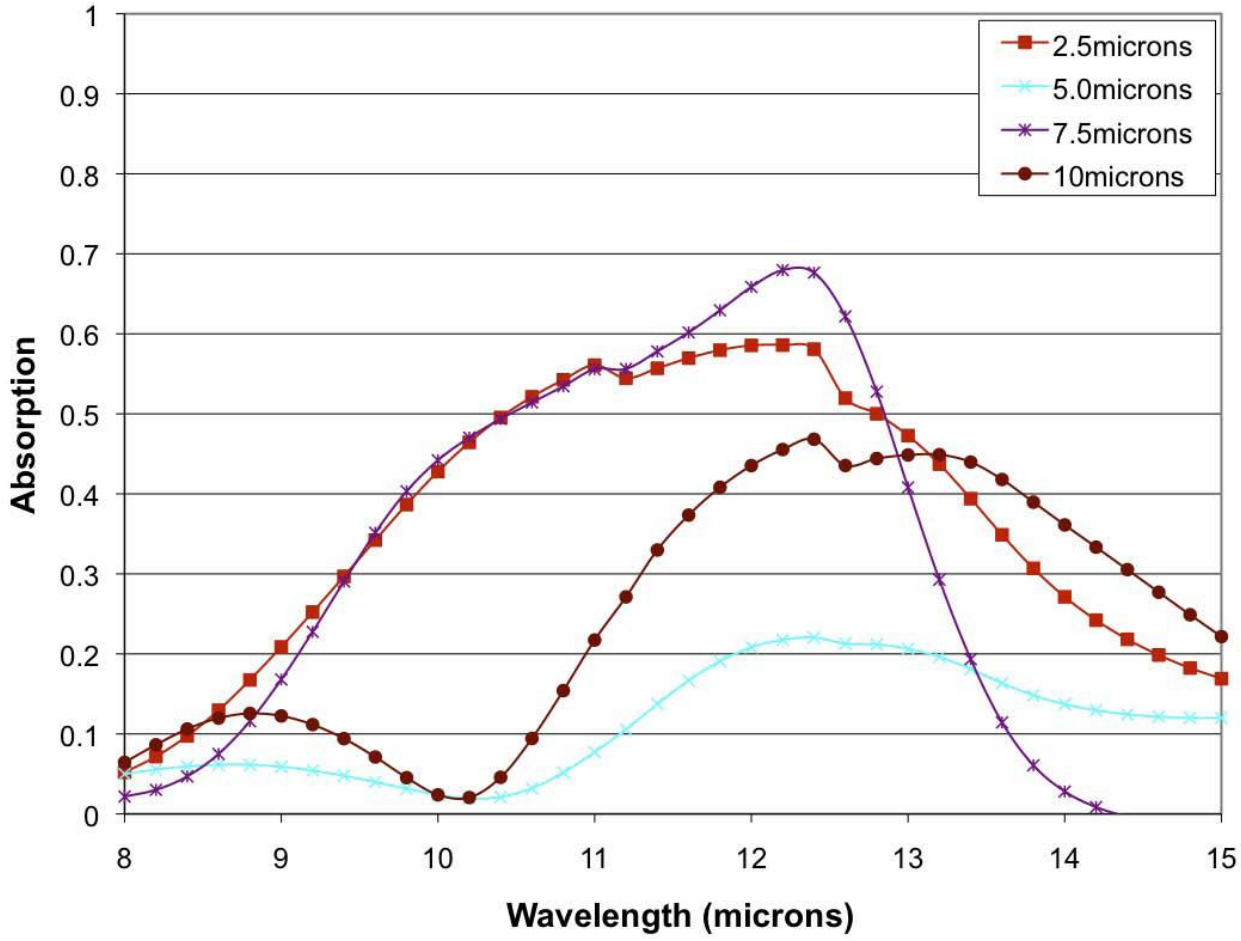

Figure 3.7: Absorption as modeled by a 3D Rigorous Coupled Wave Analysis (RCWA) for a 200nm thick 20um diameter, silicon nitride resonator above a silicon substrate. The separate plots are for different substrate to detector spacing. [3]

Chapter 3 References

[1] M. R. Watts*, et al.*, "Microphotonic Thermal Detectors and Imagers," in *Laser Resonators and Beam Control Xi*. vol. 7194, A. V. Kudryashov*, et al.*, Eds., ed Bellingham: Spie-Int Soc Optical Engineering, 2009.

[2] W. Radford*, et al.*, "Sensitivity improvements in uncooled microbolometer FPAs," in *Infrared Technology and Applications Xxv*. vol. 3698, B. F. Andresen and M. S. Scholl, Eds., ed Bellingham: Spie-Int Soc Optical Engineering, 1999, pp. 119-130.

Chapter 4 Metamaterials and VLWIR Detector Design

Metamaterials can be engineered to have resonance characteristics of unnatural materials, demonstrating the possibility for their use in detection of undeveloped spectral regions. In this chapter a description of metamaterials, as well as the subgroup of split-ring resonators, and their application to thermal detection will be presented.

4.1 Introduction to metamaterials

In 1968 V.G. Veselago theoretically explained the concept of a material possessing both negative permittivity and negative permeability [1]. He showed that such a medium would have drastically different propagation characteristics due to the sign change of the group velocity such as the reversal of both the Doppler shift and Cherenkov radiation, anomalous refraction, and even the reversal of radiation pressure and tension. This new medium causes an arrangement of the electrical and magnetic field with respect to the wave vector to be described by a left-handed Cartesian co-ordinate system, leading to the term left-handed material. Materials possessing these negative characteristics were unavailable at the time of the published paper as they do not naturally occur. More recently researchers have proven the theoretical explanations of Veselago with the creation of metamaterials. Metamaterials are engineered to create unique characteristics that are not found in naturally occurring substances/materials (negative permittivity and permeability). These materials can be constructed using nonmagnetic materials to create a periodic structure with specific optical properties. Research of metamaterials is being done for many applications such as cloaking and

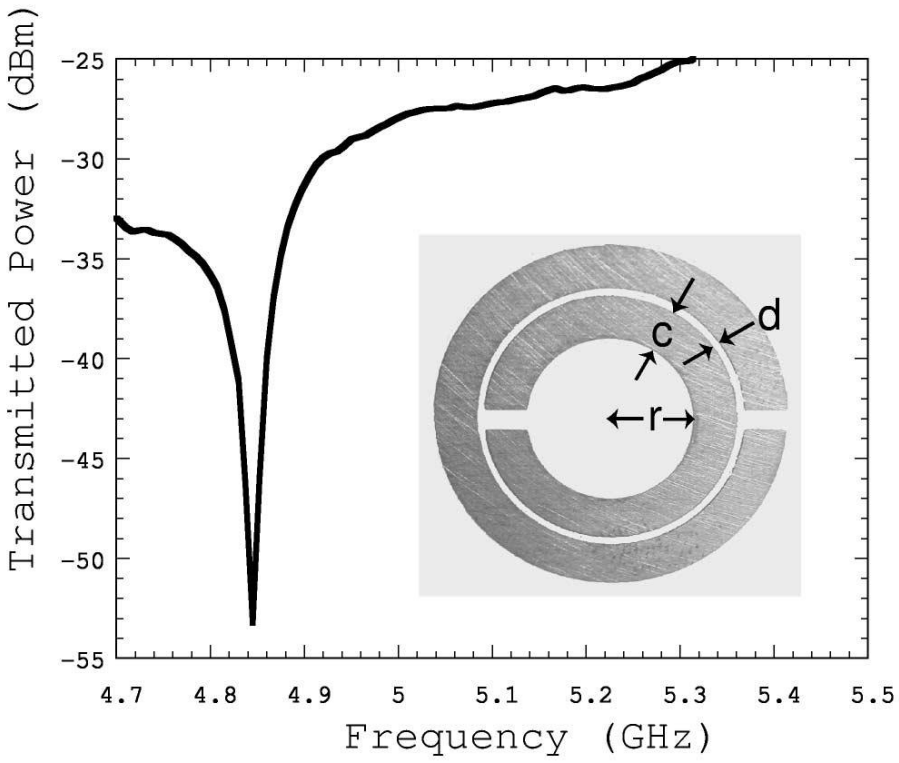

Figure 4.1: Resonance curve of SRR. Inset nested loop layout c = 0.88 mm, d = 0.2 mm, and r = 1.5 mm. [2]

antennae [3, 4]. Split-ring resonators (SRR) are a component of the metamaterial field which have negative permeability as well as electric and magnetic resonances [2]. SRRs are structured as an inductive ring split by a capacitive gap. The reason for splitting the ring is to produce resonance at wavelengths much larger than the ring itself [2]. Due to the small size of the ring, relative to the absorbed electromagnetic radiation, the radiative losses are quite small and produce high quality factors [2]. When the SRR is incident with an electric field electrically polarized across the gap, currents are induced inside of the ring. In 2000 using a nested loop design the SRR was fabricated and demonstrated. Figure 4.1 shows the nested loop design and the transmission spectrum published in reference [2]. Since the first proven SRR, many different shapes and sizes have been shown including hexagonal and square. These are some of the other highly

used orientations of SRRs [5]. The implementation of these new shapes and sizes has shown that SRRs can possess resonance in the THz and more recently in the visible regime [6, 7]. Using the resonance characteristics of metamaterials, regions, such as the so-called terahertz gap, can be targeted for detection applications.

4.2 LC and RLC Circuits

A LC circuit consists of an inductor and a capacitor. The combination of these electrical components forms an electrical resonator. The resonance is caused by the energy in the circuit being transferred from one component to the other. This is more of an ideal case as all materials possess some amount of resistance; a real world case is described by a RLC circuit consisting of a resistor, capacitor, and an inductor connected in series. In the ideal case of the LC circuit the energy continuously flows back and forth, with the introduction of resistance the energy is dissipated due to ohmic losses causing Joule heating of the circuit. Figure 4.2: Basic layout of a series RLC circuit shows a series RLC circuit where R represents the resistance of the resistor, L is the inductance of the inductor, and C is the capacitance of the capacitor.

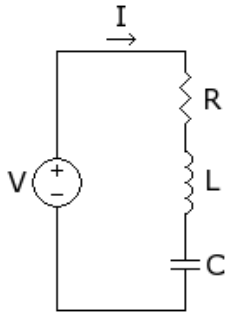

Figure 4.2: Basic layout of a series RLC circuit

The impedance of the RLC circuit expressed in the s-domain is described by Equation 4-1.

Equation 4-1

$$Z(s) = \frac{V(s)}{I(s)} = \frac{L(s^2 + \frac{R}{L}S + \frac{1}{LC})}{s}$$

Substituting $s = j\omega$ into Equation 4-1 and solving for the magnitude of the impedance results in the steady state solution (Equation 4-2), where $j = \sqrt{-1}$.

Equation 4-2

$$|Z(j\omega)| = \sqrt{R^2 + (\omega L - \frac{1}{\omega C})^2}$$

Solving for the minimal value of the impedance the resonant frequency is found, shown in Equation 4-3.

Equation 4-3

$$f_r = \frac{1}{2\pi\sqrt{CL}}$$

The current of a basic RLC circuit with values of L = 2 mH, C = 5 µF, R = 1 Ω, and V(ω) = 1 Volt is plotted in Figure 4.3.

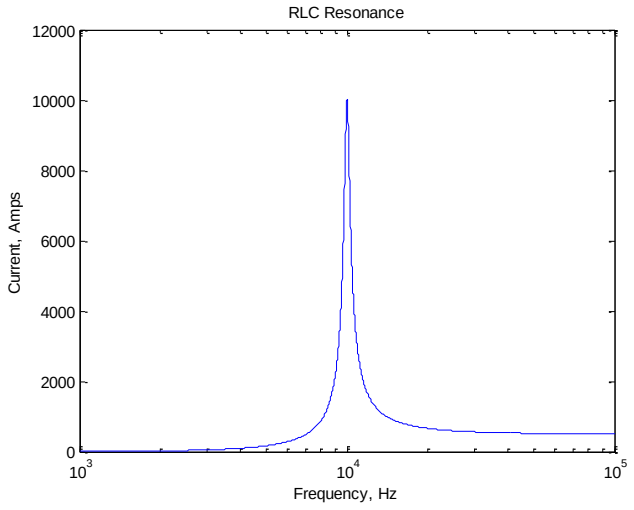

Figure 4.3: Current in a series RLC circuit, L = 2 mH, C = 5 µF, r = 1, V(ω) = 1 Volt

The SRR can be described as an RLC circuit where the resonance frequency is shown in Equation 4-3. When EM waves of the correct polarization and resonant frequency are incident on a SRR, currents are induced in the loop. The loop of the SRR can be simulated as a series inductor and resistor and the gap can be simulated as a capacitor as seen in Figure 4.4. Joule heating occurs due to ohmic losses. The heating can be taken advantage of by using a MEMs bimorph cantilever. Bimorph devices are made by placing two materials with different coefficients of thermal expansion together. When a bimorph device heats, stress is caused by the difference in thermal expansion causing the cantilever to bend.

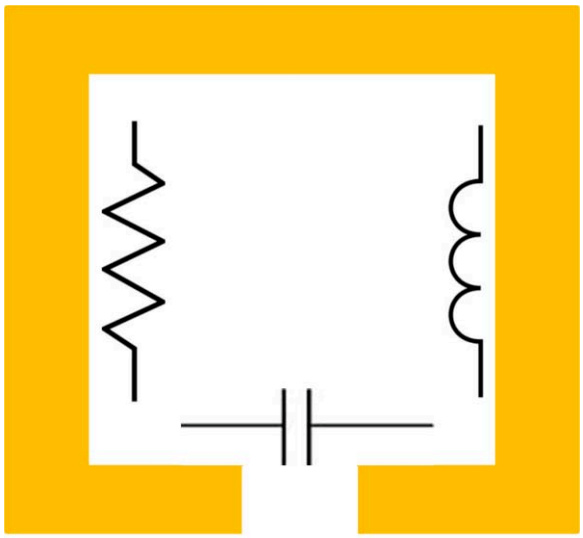

Figure 4.4: R, L, and C components of a split-ring resonator

4.3 Detector Design

Two different detectors were designed and fabricated by Boston University to incorporate bimorph cantilevers and SRRs. One designed for 95 GHz detection (microwave spectrum) and the other for 693 GHz detection (THz spectrum). The SRR for

95 GHz detection was designed as a basic square SRR, the layout of the SRR can be seen in Figure 4.6. A 50 µm x 50 µm optical pad was added for the ability to optically measure the detector using deflection readout. The SRR is fabricated onto a silicon nitride cantilever supported by two bimorph arms. At resonant frequencies small currents are induced in the SRR which will produce Joule heating. The heat will cause stress in the bimorph arms and therefore change the angle of the optical pad. The bimorph arms are fabricated by depositing gold on top of silicon nitride. The combination of the cantilever and SRR are considered a unit cell or pixel. The 693 GHz SRR was designed in much the same way as the 95 GHz SRR, except the overall size is smaller due to the shorter wavelength of resonance. The capacitance gap length was made smaller to enhance resonance, and the optical pad had dimensions of 12 µm x 20 µm. Due to the built in stress of the bimorph arms the room temperature angle of the cantilever with respect to the substrate was 50 degrees for the 95 GHz pixel and about 5 degrees for the 693 GHz pixel. The 95 GHz detector layout is shown in Figure 4.6 and a micrograph of the detector can be seen in Figure 4.7. The 693 GHz detector layout can be seen in Figure 4.8 and a micrograph is shown in Figure 4.9.

4.4 Fabrication

The detectors were fabricated on a silicon wafer coated with a 200 nm thick silicon nitride layer. A gold layer was deposited onto the silicon nitride and patterned using basic lithography to form the bimorph arms and SRR. A plasma etch was used to pattern the silicon nitride. To thermally isolate and release the pixel the silicon substrate was

removed. The process flow can be seen in Figure 4.5. The resulting pixel has a gold SRR deposited on a silicon nitride layer supported by two bimorph arms forming a cantilever.

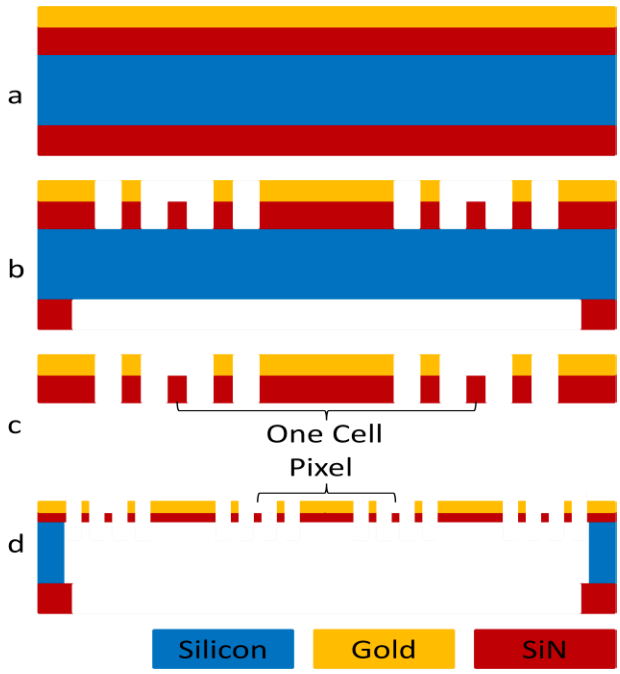

Figure 4.5: Process flow of metamaterial cantilever a) Deposition of gold onto SiN b) Pattern and etch gold and SiN_x to form pixel c) Remove silicon substrate to release cantilever d) Sample image of resultant device

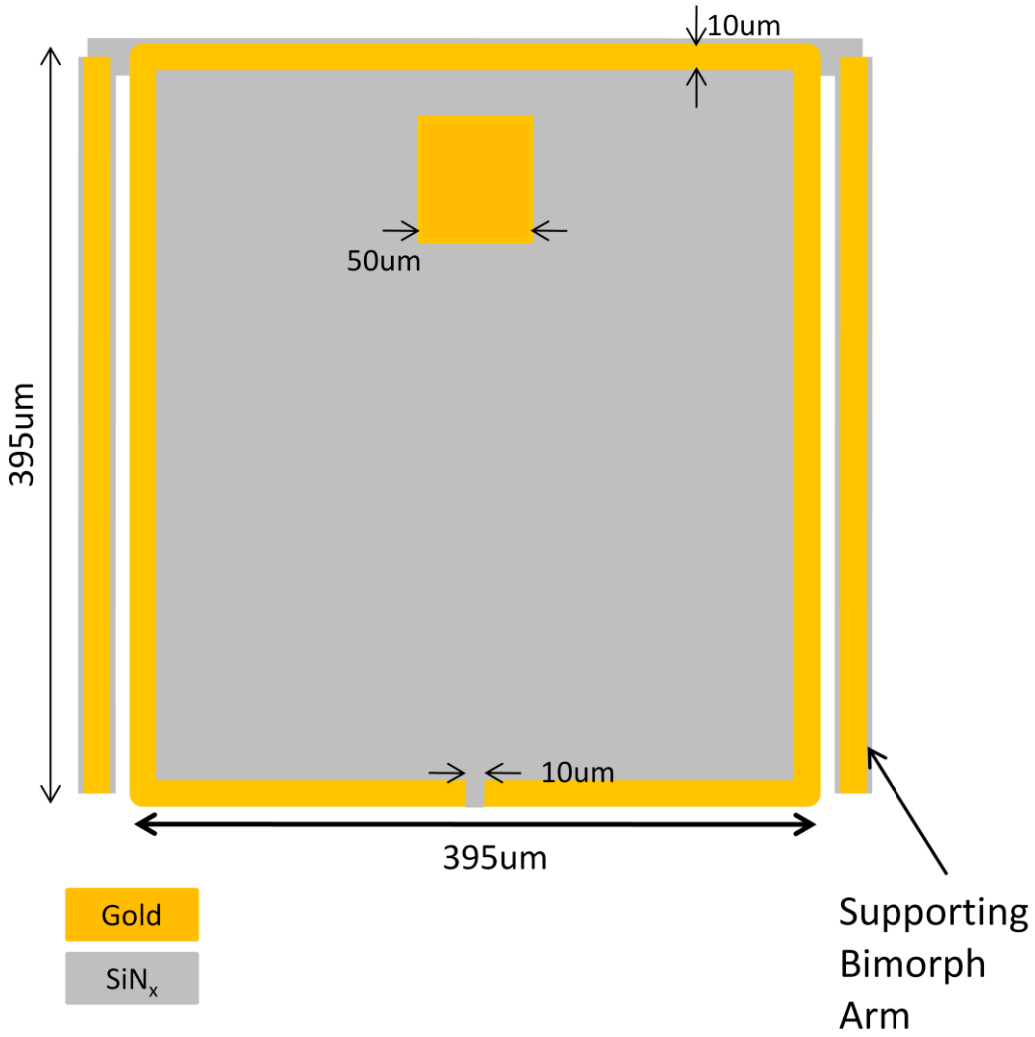

Figure 4.6: Dimensions of 95GHz Pixel

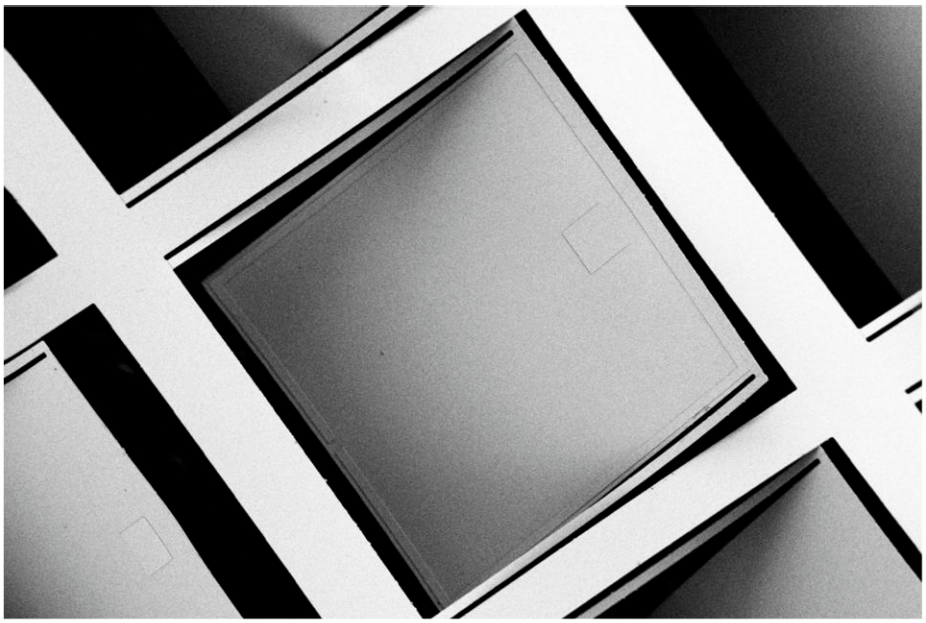

Figure 4.7: SEM image of 95GHz Pixel. Taken at Boston University

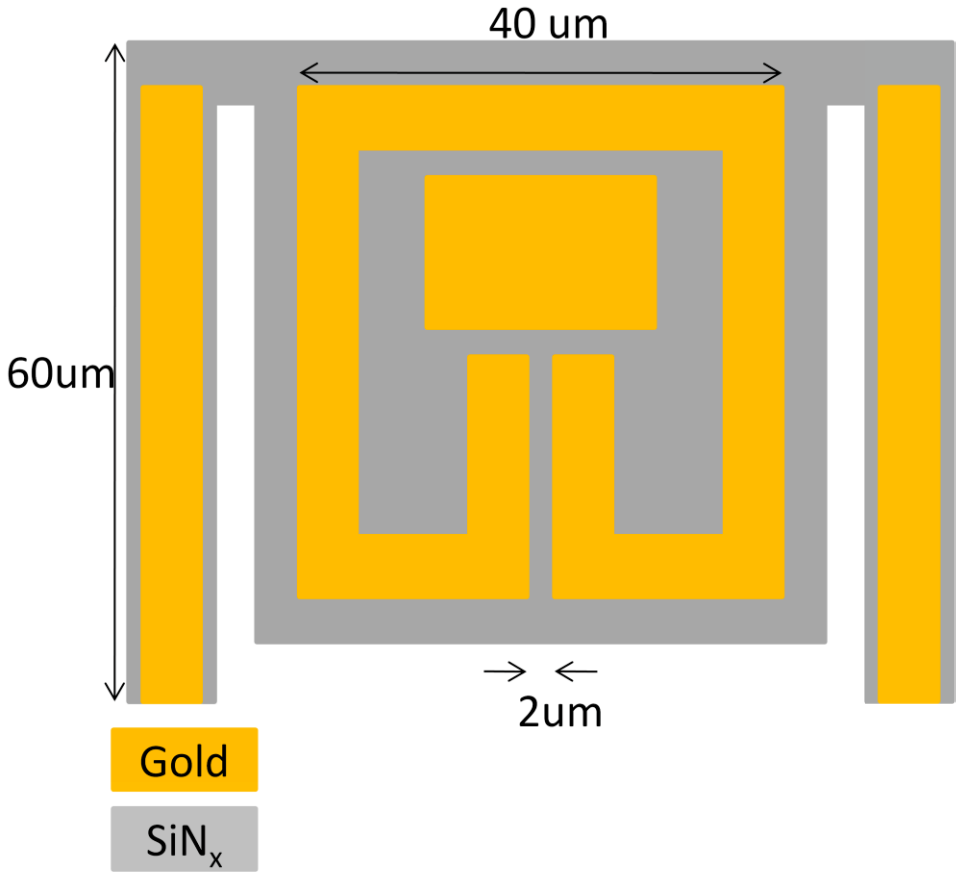

Figure 4.8: Dimensions of 693GHz pixel

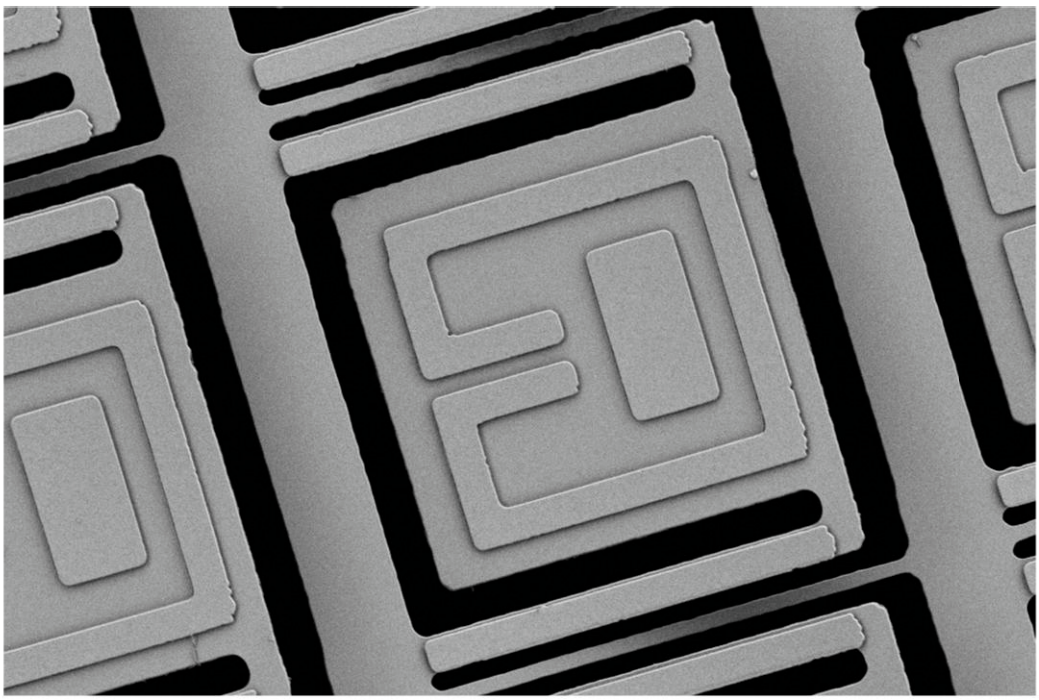

Figure 4.9: SEM image of 693GHz pixel. Taken at Boston University

Chapter 4 References

[1] V. G. Veselago, "ELECTRODYNAMICS OF SUBSTANCES WITH SIMULTANEOUSLY NEGATIVE VALUES OF SIGMA AND MU," *Soviet Physics Uspekhi-Ussr,* vol. 10, pp. 509-&, 1968.

[2] D. R. Smith*, et al.*, "Composite medium with simultaneously negative permeability and permittivity," *Physical Review Letters,* vol. 84, pp. 4184-4187, 2000.

[3] D. Schurig*, et al.*, "Metamaterial electromagnetic cloak at microwave frequencies," *Science,* vol. 314, pp. 977-980, 2006.

[4] B. I. Wu*, et al.*, "A study of using metamaterials as antenna substrate to enhance gain," *Progress in Electromagnetics Research-Pier,* vol. 51, pp. 295-328, 2005.

[5] C. M. Bingham*, et al.*, "Planar wallpaper group metamaterials for novel terahertz applications," *Optics Express,* vol. 16, pp. 18565-18575, 2008.

[6] T. J. Yen*, et al.*, "Terahertz magnetic response from artificial materials," *Science,* vol. 303, pp. 1494-1496, 2004.

[7] A. N. Grigorenko*, et al.*, "Nanofabricated media with negative permeability at visible frequencies," *Nature,* vol. 438, pp. 335-338, 2005.

Chapter 5 Metamaterial Detector Characterization

In this chapter the characterization of the metamaterial based detectors will be presented showing their workability and potential of use in thermal detection applications.

5.1 TDS transmission measurements

Terahertz Time-Domain spectroscopy (THz TDS) is a well-known and widely used method for measuring the THz response of materials. These systems used to be strictly built in house but are now commercially available. A basic TDS system consists of a transmitting and receiving antenna. Ultra short pulses of terahertz radiation probe a sample medium evaluating the transmission or reflection by measuring the change in amplitude and phase of the received signal. A Picometrix TDS system was used to measure the transmission of the 95 GHz and 693 GHz detectors and can be seen in Figure 5.1.

5.2 Optical Measurement Device

An optical measurement apparatus was built for the measurement of the 95 GHz and 693 GHz samples. This device was made using Thorlabs cage mount parts consisting of a beam collimator, 5x beam expander, beam splitter, a 20x microscope objective for focusing, and a position sensitive detector (PSD) to measure the movement of the reflected beam. This device is easily mounted on a lab jack for mobility and height adjustment. The PSD electronics were purchased from Hamamatsu. Figure 5.2 show the layout of the optical measurement device.

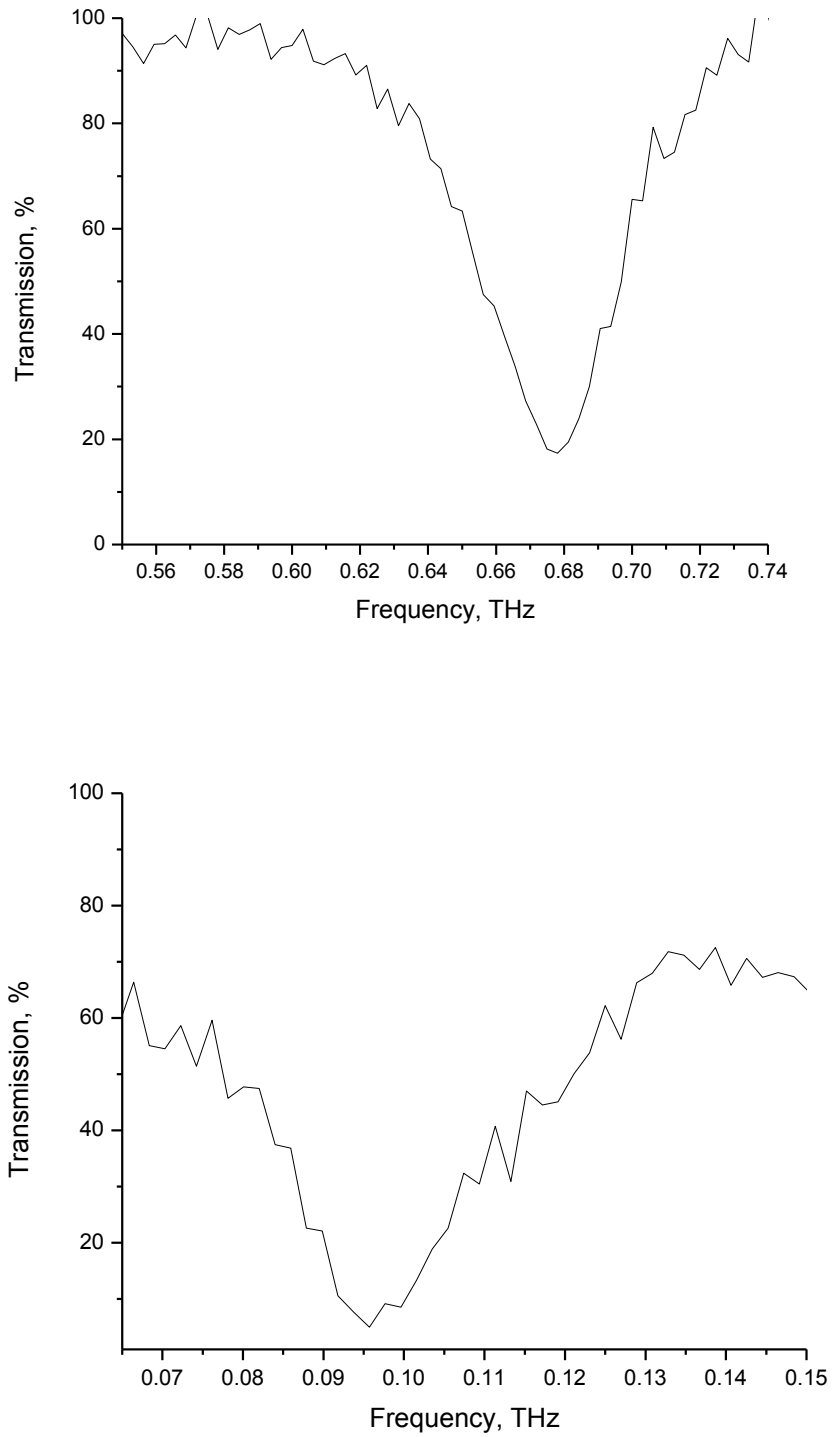

Figure 5.1: TDS transmission measurements (top) 693 GHz detector (bottom) 95 GHz detector

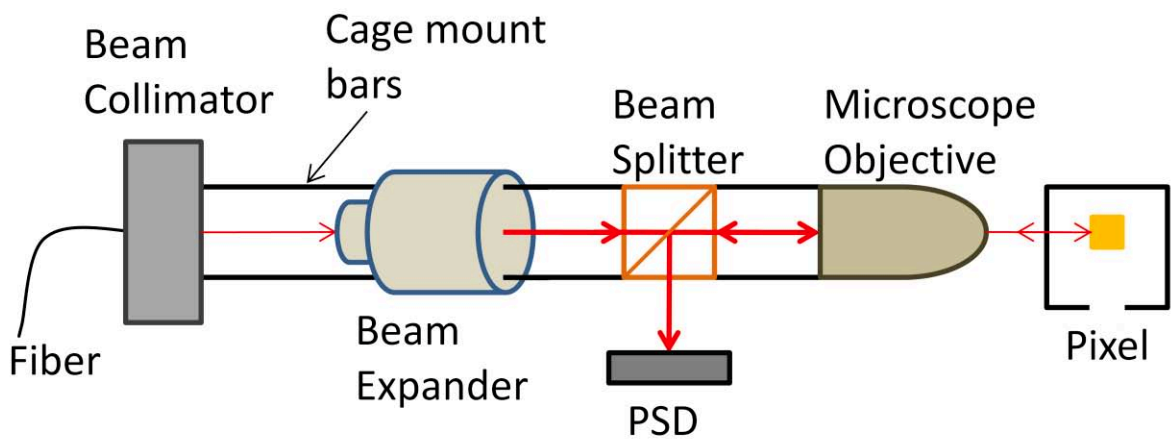

Figure 5.2: Layout of optical measurement apparatus

5.3 THz Source for 95 GHz Characterization

The THz source used for the characterization of the 95 GHz pixels was purchased from Virginia Diodes Inc. (VDI). The source consisted of an Yttrium iron garnet (YIG) oscillator with a frequency range of 20 – 40 GHz controlled by a user-supplied voltage of 0 – 10 Volts. The output of the YIG oscillator is connected to a 10 dB coupler for frequency readout. The other output connection of the coupler is connected to an amplifier which is connected to a 3x frequency multiplier. The 3x frequency multiplier is connected to another amplifier to increase the output power. This is the basic configuration which supplies a frequency range of 75 – 110 GHz. Other frequency bands may be obtained by the connection of other sets of frequency multipliers. Other possible bands include: 140 – 230 GHz, 210 – 345 GHz, 280 – 460 GHz, 420 – 690 GHz, and 700 – 1000 GHz. The VDI source also has the ability for user attenuation and the input off a TTL signal for square-wave chopping of the source. Figure 5.3 shows the layout of the VDI THz source.

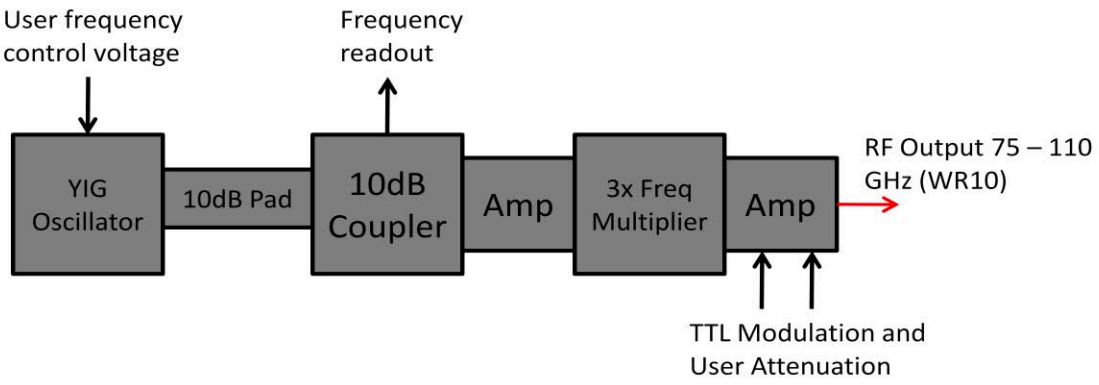

Figure 5.3: Basic setup of VDI tunable THz source

To correctly measure the response of the 95 GHz sample the power spectrum of the THz source must be known. A Thomas Keating absolute power meter was used for these measurements. Although the power was not entirely consistent the spectrum provides a good range to measure the 95 GHz sample. Figure 5.4 shows the power spectrum of the VDI THz source.

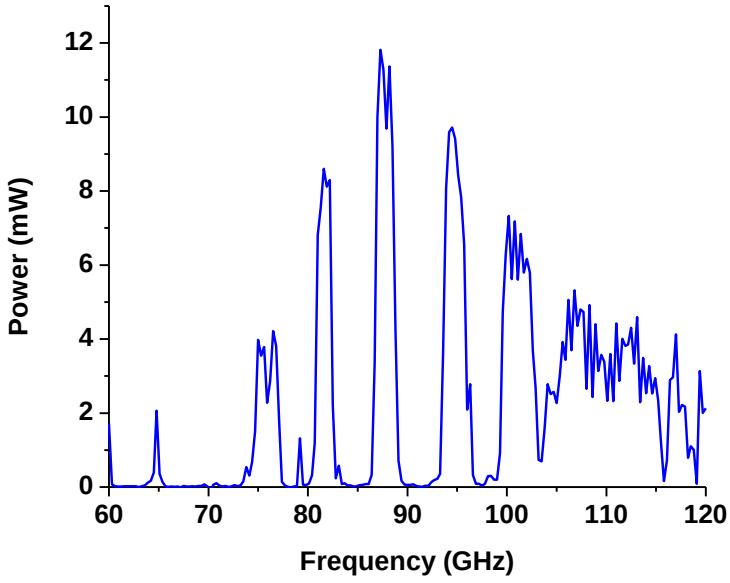

Figure 5.4: Power Spectrum of VDI THz Source

5.4 95 GHz response

A specially designed lens for W band (75 – 110 GHz) EM radiation was used to focus the THz beam onto the SRR sample. The focal length of this lens was 43 cm and the beam spot was nominally 1.1 cm. This provided ample room for equipment needed to support the sample. To hold the sample and provide a means for stabilization of the cantilever, a sample box was made with the use of two high THz transmission quartz windows and a Thorlabs cage mount box. This sample holder also provided a way to supply vacuum to the sample therefore creating higher thermal resistance of the cantilever system. Figure 5.5: Sample holder shows the sample holder.

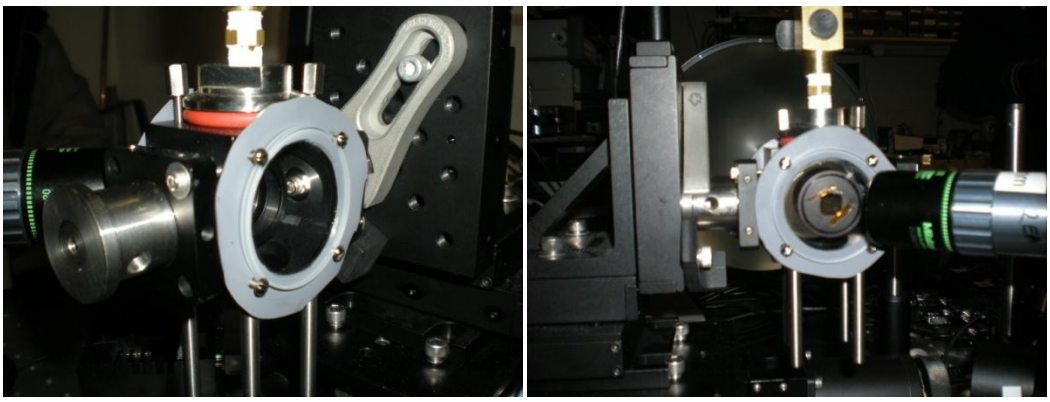

Figure 5.5: Sample holder made using ThorLabs cage mount parts and quartz windows

To ensure that the measurement beam was reflecting off of the optical pad of the 95 GHz detector a fiber light source was used to illuminate the back of the sample for viewing with the optical measurement apparatus. For viewing of the sample the PSD was replaced with a CCD camera. This image provided a view of where the measurement beam resides on the SRR and also if the optical measurement apparatus is aligned perpendicular to the SRR. Once the reflector pad is found the CCD camera is

then replaced with the PSD. The THz source was square-wave modulated using a TTL signal. A lock-in-amplifier was used to recover the signal of the detector. Due to the thermal characteristics of the device, a chopping frequency between 5 and 30 Hz was used to insure maximum thermal heating. The resonant nature of the detector was measured by scanning the frequency of the THz source and recording the optical signal of the detector. The resonance frequency was found to be 95 GHz. This value coincides with the spectrum measured using the Picometrix TDS system. To ensure proper response the polarization of the beam was rotated ninety degrees to the incorrect polarization, the optical response of the detector decreased dramatically. Figure 5.6 shows a plot of the measured optical response of the 95 GHz detector for both polarizations.

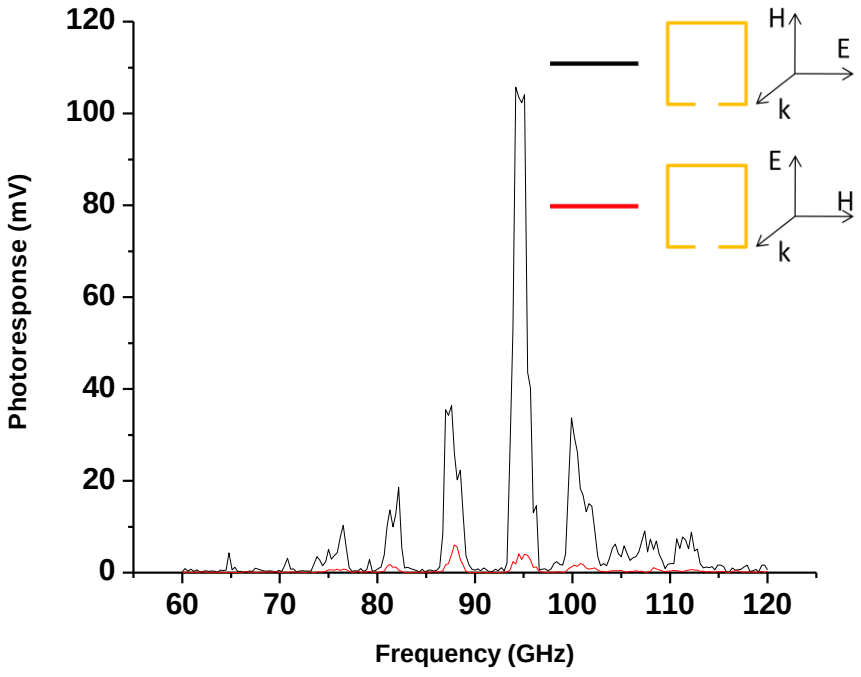

Figure 5.6: Optical response of 95 GHz detector showing resonance at 95 GHz

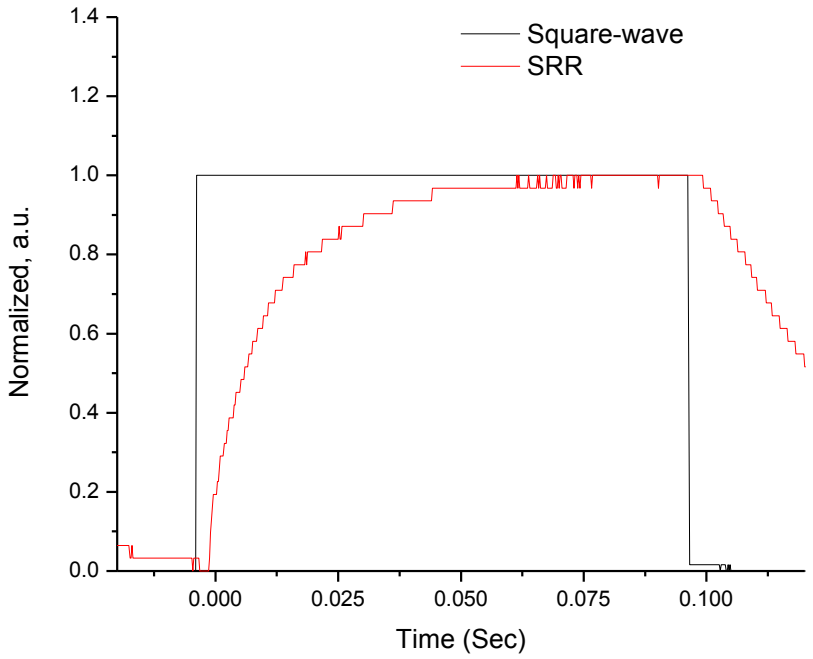

Figure 5.7: Square-wave response of 95 GHz pixel

The thermal time constant of the 95 GHz detector was found to be τ = 10 ms. For video rate applications the time constant is required to be less than 33 ms. The 95 GHz detector is well within this standard making it valid for video applications. The characteristic curve of the pixel due to square-wave pulsed incident radiation can be seen in Figure 5.7.

5.5 693 GHz Detector Characterization

For measurements of the 693 GHz device, the same optical readout scheme and sample holder were used as with the 95 GHz detector. The 693 GHz pixel, when released, has a smaller angle between it and the substrate. Due to this small angle, a different technique was used to locate the optical pad. Using Thorlabs motorized stages, a xyz-motor controlled stage was built and programmed with LabView to locate the optical

pad of a 693 GHz detector. Performing a raster scan of the transmitted measurement beam through the sample the optical pads were easily located. Figure 5.8 shows a resultant scan of the LabView program used to locate the 693 GHz detector optical pad.

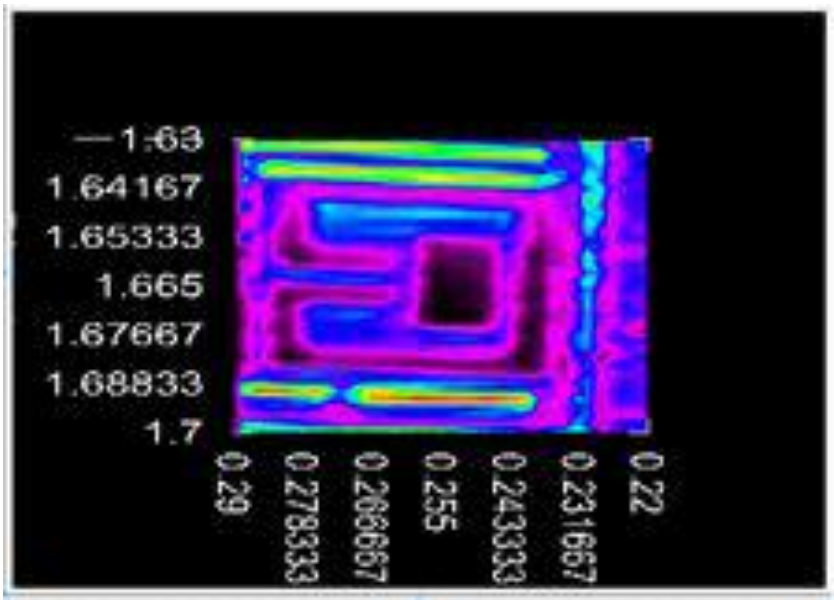

Figure 5.8: Resultant Image of Pad Location Scan, the Pad is seen in the middle of the image (X and Y axes in mm).

Although the VDI source can be used to obtain a frequency of 693 GHz it was not used because of the low power in that frequency range. Instead a far infrared laser (FIRL) based on a formic acid line pumped with a CO_2 laser was used to provide the resonant frequency. Although the frequency cannot be scanned, the FIRL provides very good power, the maximum achieved was about 10 mW. A parabolic mirror was used to focus the beam onto the sample. To show good imaging characteristics the detector must have a linear response and must be polarization dependent. Two wire-grid polarizing optics were placed together to control the output polarization and power. The output of the FIRL is polarized in the vertical direction. To provide a power sweep the second

polarizer was aligned in the vertical polarization. The first polarizer may be swept from vertical to horizontal for power attenuation. The resulting power transmitted goes as $\cos^4(\theta)$, where θ is the angle of the first polarizer referenced to the vertical plane. Figure 5.9 shows a plot of optical response vs. incident power on the detector. The noise floor of the system was 0.43 mV the reason for the offset at zero incident power. It is shown in the plot that the SRR detector has a linear response with respect to power.

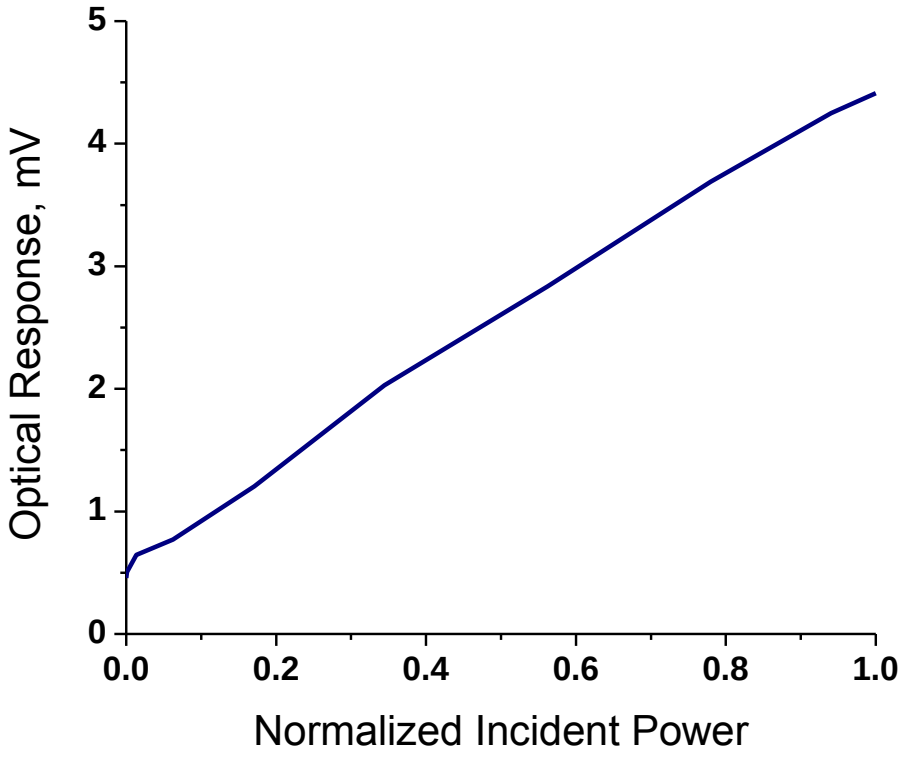

Figure 5.9: Optical power response of 693 GHz detector

The temporal response of the 693 GHz detector is plotted in Figure 5.10. The calculated thermal time constant was found to be τ = 20 ms, a larger value than the 95 GHz detector but still sufficient for video rate applications.

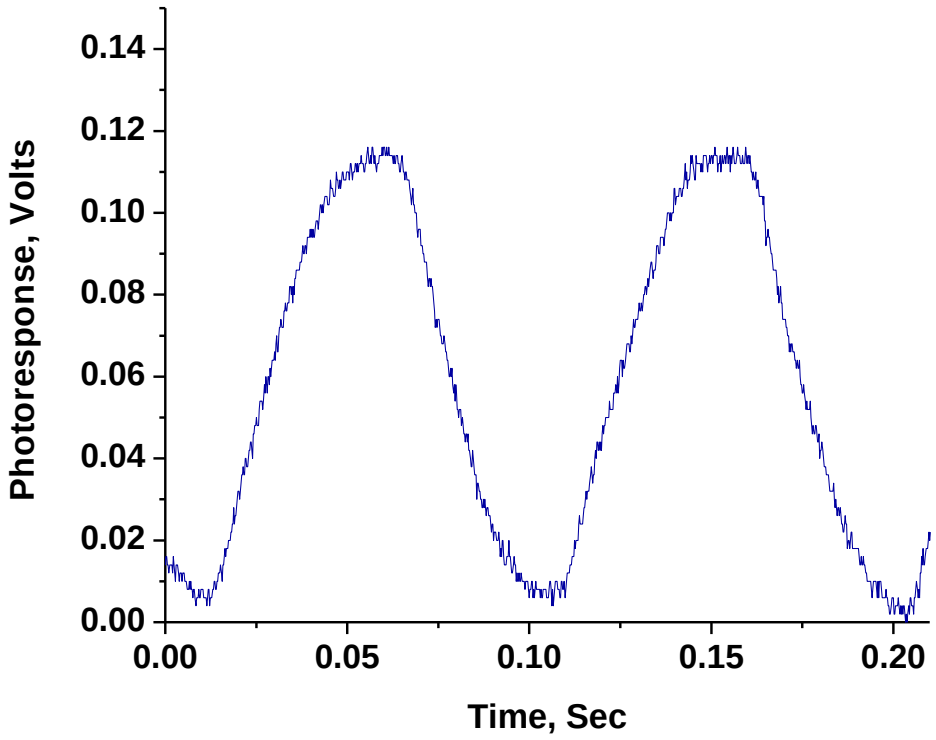

Figure 5.10: Temporal response of 693 GHz detector to incident square-wave modulated radiation

5.6 Pixel Design Improvements

To improve the pixel design more SRRs per pixel should be implemented improving the total absorbed power per pixel, therefore providing an increase of thermal sources. Currently the thermal path from the SRR to the bimorph arms is through silicon nitride which has a small thermal conductivity. To improve the speed performance of the design higher thermal conductivity material should be used to transfer the heat from

the SRR to the bimorph arms, for example gold. Figure 5.11 shows an example of a pixel layout using both of these design ideas.

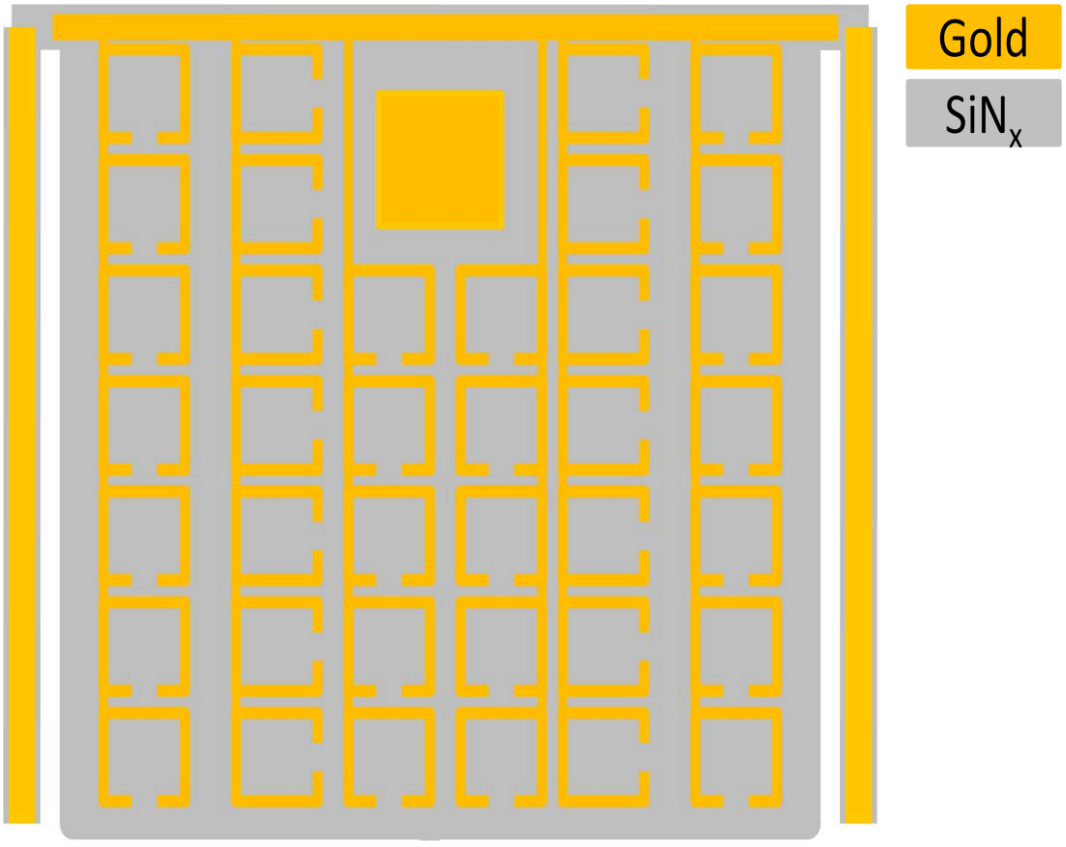

Figure 5.11: Pixel with multiple SRRs and heat sinks to bimorph arms

Chapter 6 Future Work and Conclusion

6.1 THz Beam Image

It is well known that imaging in the THz region is immature. Because of this, it is a very accessible field to employ new ideas and designs. It is ideal to have a THz detector that does not rely on ultra-fast pulsed lasers or non-linear optics, which could be implemented in an array to create an imaging focal plane. Figure 6.1 shows a beam profile taken of the FIRL beam using the 693 GHz pixel, showing the possibility for its use in beam diagnostics. The THz beam was scanned horizontally by an electronic stage and vertically by rotating a parabolic mirror to produce the image. The use of large area readout techniques such as holographic imaging or electronic speckle interferomertry could be used for measurement of a detector array to improve the required time of imaging; future work will consist of the design and fabrication of a large scale measuring device to probe multiple THz cantilever arrays.

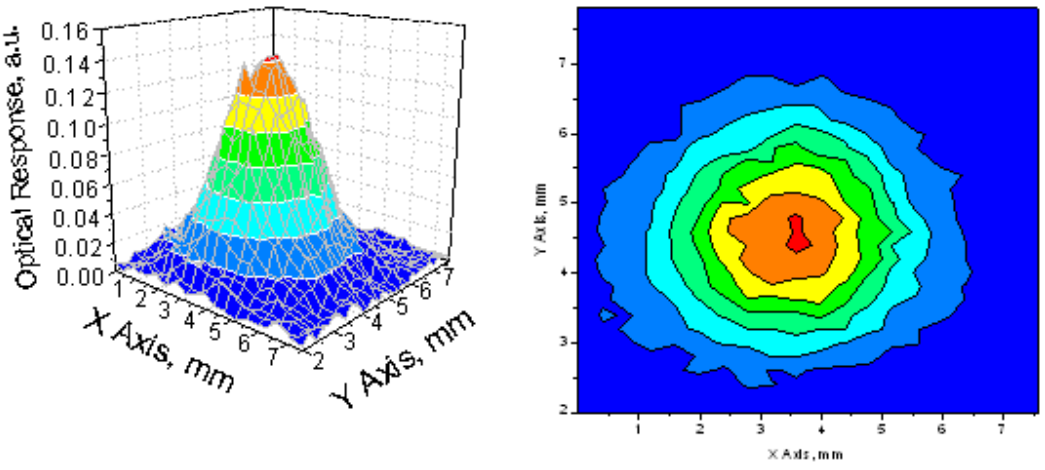

Figure 6.1: Beam profiles taken with the 693 GHz detector

6.2 Combining Metamaterials and Silicon Photonics

The combination of the microphotonic thermal detector and the SRR cantilever design could create a low-noise high-speed THz detector by placing SRRs onto the microdisk. Figure 6.2 shows examples of two possible layouts using square SRRs and hexagonal SRRs. The silicon photonic metamaterial combination could also be implemented in the improvement of thermal IR detection. Future work will consist of the design and characterization of the combination of silicon photonics and metamaterials for increased LWIR thermal detection as well as VLWIR (THz) thermal detection.

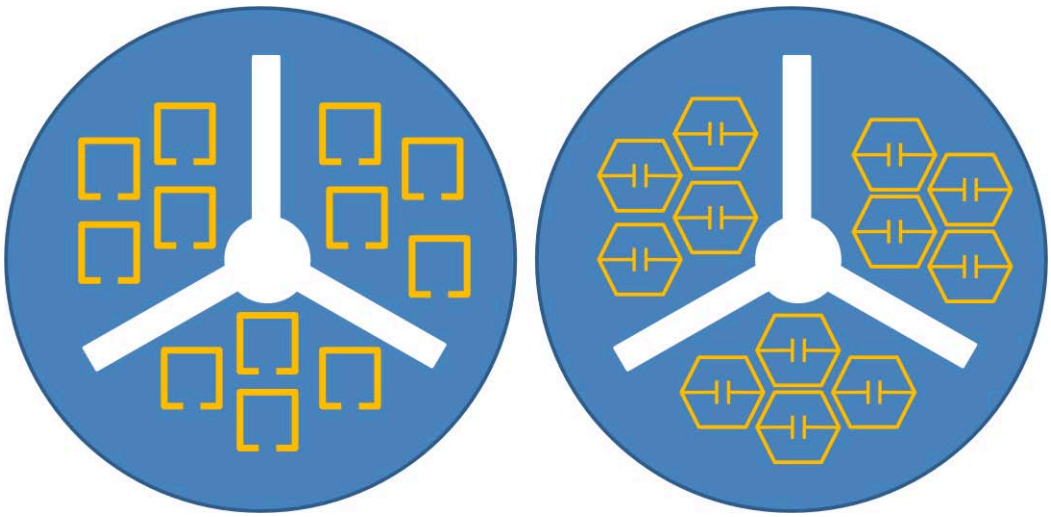

Figure 6.2: Combination of silicon photonics and metamaterials

6.3 Improving the Microphotonic Detector

As presented in chapter 3 there are many improvements to be made to the microphotonic detector. Future work will consist of evaluating the quality factor of the microdisk with different isolation tether lengths. Also included in future work is the characterization of a microphotonic detector with 3λ/4 spacing from the substrate.

These improvements, absorption and Q, should increase the detectivity of the microphotonic detector by at least an order of magnitude.

6.4 Conclusion

This thesis has shown the possibility of new detection devices in the LWIR and VLWIR regions. It was shown in chapter 3 that the microphotonic thermal detector is a good candidate to improve thermal imaging as its detectivity at early design stages is on the order of current commercially available bolometers and its thermal time constant is 5 times faster than these bolometers. With minor design changes the microphotonic detector should surpass its bolometer counterpart in detectivity by at least an order of magnitude. It was also shown, in chapter 5, that the combination of metamaterials with MEMs bimorph cantilevers can be used as a thermal detection device in the THz (VLWIR) region. These metamaterial detectors can be engineered for detection from the visible to THz regions, showing their potential for addressing the THz gap. While both of the technologies explained in this thesis can be significantly improved, this research demonstrates the potential for their application in LWIR and VLWIR detection.